1 **Revision 3**

2 Origin of gem-quality turquoise associated with quartz-barite veins in 3 western Hubei Province, China: constraints from mineralogical, fluid 4 inclusion, and C-O-H isotopic data

5 WEN-TIAN LI[1], SHAO-YONG JIANG[1*], HAO ZHANG[2], PEI-LONG CUI[2]

6 [1] State Key Laboratory of Geological Processes and Mineral Resources, Collaborative
7 Innovation Center for Exploration of Strategic Mineral Resources, School of Earth
8 Resources, China University of Geosciences, Wuhan, 430074, P.R. China

9 [2] *Eighth Geological Brigade of Hubei Geological Bureau, Xiangyang 441000, China*

10 *Corresponding author, E-mail, shyjiang@cug.edu.cn (S-Y Jiang)

11 **ABSTRACT**

12 Two types of turquoise, including homogeneous Cu-rich turquoise and oscillatory zoned
13 turquoise-planerite series, are recognized in association with quartz-barite veins hosted by Cambrian
14 carbonaceous slates from western Hubei Province of China. Combined fluid inclusion and Raman
15 microspectroscopic data reveal that turquoise-bearing barite-quartz veins contain three types of fluid
16 inclusions (pure CH_4-N_2, carbonic-aqueous, and aqueous), suggesting the responsible fluid is of
17 carbonic-aqueous composition with low oxygen fugacity. Pressure-corrected homogenization
18 temperatures in quartz and barite show a range from 325 °C to 485 °C and 186 °C to 391 °C, respectively.
19 Carbon, oxygen and hydrogen isotopic data suggest that the mineral-forming fluids have a mixed

metamorphic-organic affinity, in which the fluids have $\delta^{18}O$ and δD values of 15.0 to 18.8 ‰ and -111 to -93 ‰, respectively. Generally, the formation of quartz-barite-turquoise veins could be triggered by prior metamorphic devolatilization, followed by the interaction of fluids with country rocks enriched in carbonaceous material, which resulted in the leaching of Cu, Fe, P and Al from chalcopyrite, pyrite, magnetite, monazite, xenotime, apatite, feldspar and muscovite in the wall rocks. Decomposition of the organic matter in the carbonaceous slates, caused by regional metamorphism and deformation, could also promote the concentration and transportation of necessary metals for the turquoise. Thus, we propose a new model and suggest that the turquoise gem deposits in western Hubei Province of China belong to the non-magmatic hydrothermal vein type deposit, not the previously proposed supergene origin. The turquoise-forming fluids were characterized by the coexistence of two immiscible fluids of non-magmatic affinity (i.e., moderate to high temperature and low salinity aqueous fluid and pure CH_4-N_2 fluid formed by interaction with carbonaceous slates). The bluish green homogeneous turquoise in the metamorphic quartz-barite-turquoise veins evolved towards the turquoise-planerite solid solution series as the metal-leaching capability of the aqueous fluids decreased.

Keywords: turquoise, fluid inclusions, H-O-C isotopes, metamorphic hydrothermal origin, western Hubei Province

INTRODUCTION

The name turquoise is derived either from the French *Turquois* for Turkish, or possibly from the French *pierre turquin* (King, 2002). Turquoise is a hydrated copper aluminum phosphate and belongs to the turquoise group, consisting of aheylite, chalcosiderite, faustite, planerite and turquoise. All of them

crystallize in triclinic system with the general formula $A_{0-1}B_6(PO_4)_4(OH)_8 \cdot 4H_2O$, where Zn^{2+}, Cu^{2+}, and Fe^{2+} occur at the A site and Al^{3+}, Fe^{3+}, and Cr^{3+} replace each other at the B site (Abdu et al., 2011; Jomeh et al., 2020). Turquoise is well known as a valuable gemstone for its impressive color and thus used for rituals, demonstrating social status and adornments (Fritsch et al., 1999). The oldest turquoise deposit has a history going back 70 centuries to ancient Egypt (Fritsch et al., 1999) and for now commercial sources of this gemstone are mainly exploited from Iran, United States, Egypt, Russia, Chile, South Africa, and China. Several minerals may resemble turquoise and are commonly known as semi-precious turquoise simulants. These include malachite ($Cu_2(OH)_2CO_3$) and a fairly unusual, green variety of lazulite ($MgAl_2(PO_4)_2OH_2$) (King, 2002). Chrysocolla ($(Cu,Al)_2H_2Si_2O_5(OH)_4 \cdot nH_2O$) and dyed howlite ($Ca_2B_5SiO_9(OH)_5$) have also been used to imitate turquoise (Bernardino et al., 2016). Finally, amazonite ($KAlSi_3O_8$), a variety of microcline, can also be used to forge turquoise (Kile and Eberl, 1999; Bernardino et al., 2016).

Comprehensive research has concentrated on the mineralogy of the turquoise-group minerals (Fritsch et al., 1999; Taghipour and Mackizadeh, 2014; Dumanska-Slowik et al., 2020). Their compositional evolution during the ore-forming process, although critical for commercial exploitation, has rarely been studied in detail. Gem-quality turquoise of uncertain origin has been reported by Chen et al. (2012), Cejka et al. (2015), Rossi et al. (2017) and Dumanska-Slowik et al. (2020) from Iran, the United States and China. Previous researchers have suggested that this gemstone originates, in general, from: (1) supergene processes (meteoric water migrates along crack and fractures, leaching mineral-forming elements; Qin et al., 2015; Chen et al., 2012; Shi and Cai, 2011); (2) hydrothermal processes; and (3) hydrothermal-metasomatic processes. The hydrothermal turquoise (Type 2) precipitates from fluids which are enriched in Cu, Fe, Al and P from magmatic fluids, such as those from

63 porphyry intrusions. This type of turquoise can occur as nodules and veinlets in fractures, or in the
64 cavities of quartz in the intrusive and volcanic rocks (Disbrow and Stoll, 1957; Szakáll et al., 2012). The
65 generation of the hydrothermal-metasomatic turquoise (Type 3) could be linked to the interactions
66 between hydrothermal fluids and wall rocks containing copper-bearing phases. Such a type of turquoise
67 can also form as a result of the neoformation from preexisting minerals during reaction between
68 phosphates (e.g., montebrasite) and copper-bearing fluid (Pirard et al., 2007; Ribeiro et al., 2021).

69 Turquoise deposits in western Hubei Province of China, which occur mainly in Lower Cambrian
70 carbonaceous slates, are regarded as a significant gem source with superior quality. These account for
71 the majority of China's total turquoise production. However, the mineralogical evolution, derivation, and
72 characteristics of the fluids that control the crystallization of gem turquoise remain open questions.

73 The representative turquoise deposit within the carbonaceous slates studied here is located at
74 Zhushan County of western Hubei Province, which shows gem-level quality and has over 800 t ore
75 reserves with an annual production from 50 to 129 t (Chen et al., 2012). In this paper, we present the
76 geological, electron probe micro-analysis and laser ablation (LA) ICP-MS imaging analysis on the
77 turquoise-group minerals combined with the fluid inclusions and stable isotope (H-O-C) data of the
78 co-existing gangue minerals including barite and quartz, to better understand the formation of gem
79 turquoise. Previous research speculated that the formation of the turquoise in Zhushan County can be
80 ascribed to supergene processes involving the circulation of meteoric water along the fractures and
81 fissures, followed by leaching the mineral-forming elements (i.e., Cu, P, and Al) from the host rocks
82 (Jiang et al., 1983; Tu, 1996, 1997; Qin et al., 2015; Liu et al., 2020). Our results reconsider the
83 turquoise as a non-magmatic hydrothermal mineral which is most likely formed by the interaction of
84 metamorphic fluids, characterized by low salinity and moderate to high temperature, with organic matter

85 from wall rocks. The results allow us to propose a new genetic type named the non-magmatic
86 hydrothermal quartz-vein type turquoise deposit worldwide.

87 ## REGIONAL AND DEPOSIT GEOLOGY

88 The Qinling orogenic belt is distributed in the central segment of the Central China Orogenic Belt
89 which was formed by the late Triassic collision of the North China Block (NCB) and the Yangtze Block
90 (YB) (Fig. 1a; Chen et al., 2009). The Qinling orogenic belt, separated by the San-Bao Fault to the north
91 and the Longmenshan Fault to the south, can be further subdivided into: (1) the Huaxiong Block as the
92 southern margin of the NCB; (2) the north Qinling accretionary belt; (3) the south Qinling orogenic belt;
93 and (4) the northern margin of the YB or the Songpan fold belt by the Luanchuan Fault, the Shang-Dan
94 Fault and the Mian-Lue Fault from north to south (Fig. 1b; Li et al., 2015).

95 The Zhushan turquoise deposit studied here is located in the southwestern fragment of the Wudang
96 Block which is one of the Precambrian crystalline basements of the south Qinling orogenic belt (Zhang
97 et al., 1995). The Wudang Block is mainly composed of the Neoproterozoic Wudangshan Group which
98 is unconformably overlain by the early Neoproterozoic Yaolinghe Group, late Neoproterozoic
99 Doushantuo and Dengying Formations, and Paleozoic sedimentary rocks (Fig. 1c; Ling et al., 2002; Yue
100 et al., 2014). The Wudangshan Group comprises a suite of greenschist facies metamorphosed
101 volcanic-sedimentary rocks (Zhang et al., 2002). The early Neoproterozoic Yaolinghe Group occurs
102 along the western edge of the Wudang Block and contains greenschist facies metamorphosed
103 quartz-keratophyre tuff and pebbly tuff (Zhang et al., 2001). The late Neoproterozoic Doushantuo and
104 Dengying Formations contain limestone, dolomite, sericite schist, and phyllite (Yue et al., 2014).

105 The Wudang Block has undergone multiple deformation events, leading to the formation of NNW-

106 trending folds and faults followed by the nearly EW- and NW-trending faults, produced by continental
107 collision between the NCB and YB and local extension in the Early Paleozoic and Jurassic-Early
108 Cretaceous (Hu et al., 2002; Zhang et al., 2019). Felsic intrusions are rarely observed in the region,
109 while mafic dykes emplace into the Wudang Group along the NNW- and NW-trending faults and have
110 undergone greenschist facies metamorphism as the result of continental collision (Zhou et al., 1998;
111 Ling et al., 2007; Li and Zhao, 2016; Nie et al., 2016).

112 The turquoise deposits in the western Hubei Province are currently divided into three ore belts,
113 where turquoise deposit in Zhushan County belongs to the south one (Fig. 1c; Tu, 1996). Lin et al. (2006)
114 delineated the Cu-Ag-turquoise prospective districts in the north of the Fangshan-Zhushan Fault on the
115 basis of the metallogenic geological conditions. They also linked the Ag-Cu-Zn geochemical anomalies
116 to the regional dynamic metamorphism contributing the enrichment of copper, silver and ore-forming
117 elements. Moreover, the Fangshan-Zhushan Fault was thought to significantly facilitate the migration of
118 ore-forming fluids as conduits (Fig. 1c).

119 In particular, the distributions of the turquoise deposits are controlled by the strata of the Lower
120 Cambrian Shuigoukou Formation (Fig. 1c). The Lower Cambrian Shuigoukou Formation is subdivided
121 into two lithologic members. The lower part is composed of sericite quartz schist and siliceous rock
122 interbedded with the carbonaceous slate with phosphatic nodules. The upper lithologic member is
123 dominated by the limestone, interbedded with a small amount of mudstone (Li et al, 2012; Zhang et al.,
124 2019). The majority of turquoise ores mainly distribute in the carbonaceous slates with phosphate
125 nodules in the lower part of the Shuigoukou Formation.

126 The turquoise ore bodies occur in 20 to 100 m length and 1 to 25 m width in the carbonaceous slate
127 layers, and the largest one is about 250-m-long and 10-m-wide. Turquoise in Zhushan County has two

occurrences: (1) quartz-barite vein, and (2) disseminated in the carbonaceous slates. The former mineralization (1) is typically hosted in continuous quartz-barite veins controlled by the faults and fractures along or cross-cutting the bedding planes of the carbonaceous slates, showing sharp contact between the veins and the wall rocks (Fig. 2a). The quartz-barite-turquoise associations not only occur as elongated lenses and/or veins, but also remain in concordance with the foliations of the carbonaceous slates (Fig. 2b), suggesting a ductile deformation regime during the coeval precipitation of quartz, barite and turquoise (Li et al., 2014). The disseminated turquoise (2) is characterized by massive structure and occurs as the block-shaped aggregates outside of the quartz-barite veins, of which synchronous ductile deformation is also noticed accompanied with the mineralization (Fig. 2c, d).

METHODS

Scanning electron microscope

A JEOL JCM-7000 environmental scanning electron microscope (SEM) fitted with an energy dispersive spectrometer (EDS) system was used to identify textural and compositional features of the carbonaceous siliceous slate and turquoise at the Collaborative Innovation Center for Exploration of Strategic Mineral Resources (CIC-ESMR), China University of Geosciences (Wuhan). Back-scattered electron (BSE) images were taken to distinguish compositional zonation of turquoise and mineral assemblages in the carbonaceous slates.

Electron probe microanalysis

Major element measurements of the turquoise group minerals were carried out at the State Key Laboratory of Geological Processes and Mineral Resources, China University of Geosciences (Wuhan) (GPMR-CUG), with a JEOL JXA-8100 Electron Probe Micro Analyzer (EPMA) equipped with four wavelength-dispersive spectrometers (WDS). Standards and samples were analyzed by 20 μm spot size

150 at an accelerating voltage of 20 kV and a beam current of 5 nA. Data were corrected on-line using a
151 ZAF (atomic number, absorption, fluorescence) correction procedure. H_2O contents were calculated by
152 difference of analytical total to the 100 wt.% and then incorporated into the ZAF correction procedure.
153 The peak counting time was 10 s for Al, P, Si, S, Cu, Fe, K and 20 s for Zn, Sr, Cr, Ti, V, Ti, Y, U and Ba.
154 The background counting time was one-half of the peak counting time on the high- and low-energy
155 background positions. The peak overlap of Ti K_β on V K_α and V K_β on Cr K_α was corrected by the
156 interference correction program provided by the Japan Electron Optics Laboratory (JEOL) during the
157 analysis. The following standards were used: pyrope garnet (Fe, Al), apatite (Ca, P), sphalerite (Zn),
158 olivine (Si), barite (S), copper (V), sanidine (K), chromium (Cr), vanadium (V), rutile (Ti), barium
159 fluoride (Ba), uranium (U). The calculation of their crystal-chemical formula was based on the 11
160 cations following the general formula from Foord and Taggart (1998).

161 **LA-ICP-MS mapping**

162 LA-ICP-MS analysis was undertaken at the CIC-ESMR, China University of Geosciences (Wuhan),
163 using NWR 193 HE laser ablation system and He-Ar carrier gas (ca. 1.2 L min^{-1} He and ca. 0.9 L min^{-1}
164 Ar) coupled to an Agilent 7900 single quadrupole ICP mass spectrometer. A trace element map was
165 constructed from the sequential line analyses under the following conditions: laser beam size ($Ø_{spot}$) of 5
166 μm, scan speed (V_{scan}) of 17 μm/s, repetition rate of 20 Hz, and the total dwell time (T_{acq}) of 147 ms,
167 corresponding a high X-spatial resolution of 7.5 μm calculated from the following equation:

168 $$X_{resolution} = Ø_{spot} + V_{scan} \times T_{acq} \quad (1)$$

169 Each line analysis was composed of 10 s for background signal acquisition before the line ablation and
170 10 s for washout after the line analysis on the basis of a fast washout system (70% signal reduction in

less than 0.4 s). Further detailed analytical processes are similar to those described by Ubide et al. (2015). NIST 610 glass was used as a calibration standard which was determined twice at the beginning, middle and end of the analysis under the same parameters relative to the 84 unknown lines for the entire mapping. Data reduction of trace elements distribution map was carried out by software Iolite v2.5 under semi-quantitative mode, using NIST 610 as the external standard.

Fluid inclusion analysis

Microthermometric determinations on a total of 134 fluid inclusions were carried out on doubly polished 100-μm-thick sections, using a Linkham THMS-600 Heating-Freezing Systems (from -196 °C to 550 °C) attached with a Zeiss AX-1 microscope at the CIC-ESMR, China University of Geosciences (Wuhan). The stage was calibrated with synthetic fluid inclusions at -56.6 °C, 0.0 °C and 374.1 °C supplied by SYN FLINC. The accuracy of the systems was ± 2.0 °C for homogenization temperatures and ± 0.2 °C during the freezing cycle.

Laser Raman spectroscopic analyses of the individual inclusion were performed on a Renishaw RM-1000 Raman spectrometer attached with a 514.5-nm Ar ion laser operating at 5mW as the source of excitation at the GPMR-CUG. The analysis of the inclusions was undertaken by the spectra from 1200 to 3800 cm^{-1} with an accumulation time of 30 s per scan and a spectral resolution of 1 to 2 cm^{-1}. The longpass Rayleigh filter was 785 nm. All spectra were collected with the 1800 groove/mm grating, and a 20× objective or a 50× long working distance objective. Raman data were processed using the Labspec6 software (Horiba Jobin Yvon). The baseline subtraction was first operated automatically at the degree of 5-8 in the Labspec6 software. Peaks were then searched and fitted using Gaussian-Lorentzian functions with the level of 10 and the size of 30 according to the spectroscopic half width and peak intensity. The

This is the peer-reviewed, final accepted version for American Mineralogist, published by the Mineralogical Society of America.
The published version is subject to change. Cite as Authors (Year) Title. American Mineralogist, in press.
DOI: https://doi.org/10.2138/am-2022-8643. http://www.minsocam.org/

192 laser beam size was 1 μm in diameter. Raman spectra and particular band assignments of individual fluid
193 inclusion as well as relevant references were listed in the Table 3.

194 **Stable isotope analysis**

195 Oxygen isotopic compositions of quartz and hydrogen and carbon isotopic compositions of the
196 fluid inclusions in quartz were determined at the analytical laboratory of Beijing Research Institute of
197 Uranium Geology (BRIUG), China, using a MAT253 mass spectrometer. Two Qtz^{I} samples dominated
198 by the primary and pseudosecondary type I and type II inclusions and one Qtz^{II} sample dominated by the
199 type II and III inclusions were picked out from hand specimens and ground to about 60 mesh. Separated
200 quartz grains were cleaned by pure 6 N nitric acid to remove other minerals and organic matter and were
201 rinsed with deionized water. Oxygen was liberated from quartz by quantitatively reacting with pure BrF_5
202 and heating with a CO_2 laser, following the method of Clayton and Mayeda (1963). For H and C isotope
203 analysis of fluid inclusions in quartz, grains were first heated at 150 ºC for over 4 h to remove surface
204 water and water from the secondary fluid inclusions. Then, mixed gases were released and collected
205 under vacuum after the decrepitation of heated quartz above 550 °C; H_2 was obtained from the reaction
206 of H_2O and zinc at 800 °C. Mixed CO_2 and CH_4 were also collected, frozen by liquid nitrogen, and
207 separated by adsorbed materials for $\delta^{13}C$ measurement using the method of Jin et al. (2021). The H-O
208 isotope data were reported relative to Vienna-Standard Mean Ocean Water (V-SMOW) with internal
209 precisions of better than 1 ‰ for δD and 0.2 ‰ for $\delta^{18}O$ of a single analysis. Oxygen isotopic
210 compositions in hydrothermal fluids were calculated following the equation:

211 $$1000 \times \ln\alpha_{quartz-water} = 3.38 \times \left(10^6 \times T^{-2}\right) - 3.40 \quad (2)$$

212 where T in Kelvin (K) is the average pressure-corrected homogenization temperature from fluid

inclusion measurement as shown in Table 4, and α represents the equilibrium constant between the quartz and fluid at a given temperature.

RESULTS

Sample characterization

Disseminated turquoise occurring as blocks and anhedral masses in the country rocks has bluish green color and shows a waxy luster (Fig. 3a). On the other hand, turquoise distributed in the metamorphic quartz-barite veins along or cross-cutting stratigraphic horizons is characterized by either bluish green (Fig. 3b) or light green color (Fig. 3c, d) as well as vitreous and waxy luster. At the microscale, two types of turquoise were further recognized in the transmitted-light photomicrographs (Fig. 4a). The quartz-barite-turquoise veins and carbonaceous slates comprise the homogeneous bluish green turquoise (Trq^{I}) in 3-5 mm which is mostly intergrown with euhedral barite (Brt^{I}), surrounded by quartz (Qtz^{I}) (Fig. 4a). Additionally, quartz-barite veins contain light-green Trq^{II}, characterized by more transparent crystal surface. Trq^{II} replaces the Trq^{I} along the crystal margin and is cut by fine-grained irregular (anhedral) barite veins (Brt^{II}) as shown in Fig. 4a, suggesting both Trq^{II} and Brt^{II} are paragenetically later. Even though Qtz^{I} and Qtz^{II} show less variations in terms of their textures, they could be successfully distinguished according to the characteristics of the enclosed fluid inclusions as described later. Back-scattered electron (BSE) images of the bluish green turquoise in the country rocks and veins (Fig. 3a, b) show that all the Trq^{I} samples are non-turbid, homogeneous, and mineral inclusions free (Fig, 4b). The Trq^{I} intimately contacts with the Qtz^{I} and Brt^{I} grains along smooth, wave-like boundaries, and there is no cross-cutting, alteration or dissolution observed in their contact zones. Light green Trq^{II} (Fig. 3c, d) in quartz veins shows well defined oscillatory zonation and coexists

This is the peer-reviewed, final accepted version for American Mineralogist, published by the Mineralogical Society of America.
The published version is subject to change. Cite as Authors (Year) Title. American Mineralogist, in press.
DOI: https://doi.org/10.2138/am-2022-8643. http://www.minsocam.org/

234 with Qtz^{II}, which is filled with anhedral Brt^{II} according to the BSE images (Fig. 4c).

235 In petrographic observations of the thin sections, the carbonaceous slate is composed of micro-fine
236 to fine-grained quartz and muscovite, and medium-grained magnetite and pyrite (Fig. 4d-h). The
237 deformed carbonaceous slate presents a lamination determined by quartz and muscovite framework with
238 a strongly-developed foliation defined by alignment of elongated magnetite and fine-grained muscovite
239 (Fig. 4d, e). The mineralogy of the carbonaceous slates includes quartz, anhedral coarse-grained barite,
240 and apatite, with subordinate muscovite, distributed as fine flakes in the quartz (Fig. 4f, g).
241 Medium-grained pyrite occurs as disseminated euhedral to subhedral grains in the quartz or is
242 overprinted by the medium to coarse-grained magnetite and barite (Fig. 4f). Monazite, rutile and
243 xenotime are common but less abundant in the carbonaceous slate (Fig. 4h). Rock-Eval pyrolysis and
244 the separation of soluble organic compounds of the carbonaceous slates have been conducted by Wang
245 (2009) which illustrated that the carbonaceous matter is mainly composed of kerogen with a small
246 amount of the hydrocarbons from the kerogen decomposition due to the thermal evolution. Yields of
247 extractable soluble organic matter in the host rocks are fairly low in the range of 15.0 and 142.0 mg/g,
248 which might be attributed to the high thermal maturity of the organic matter in these rocks (Hu et al.,
249 2000).

250 **Chemical compositions**

251 Detailed EPMA compositional determination and the unit formula (apfu) of the turquoise group
252 minerals are summarized in Table 1. Major element analysis of samples collected from Zhushan County
253 indicates they belong to turquoise-planerite solid solution series.

254 Trq^{I} within the carbonaceous slate and the quartz-barite veins display similar chemical

This is the peer-reviewed, final accepted version for American Mineralogist, published by the Mineralogical Society of America.
The published version is subject to change. Cite as Authors (Year) Title. American Mineralogist, in press.
DOI: https://doi.org/10.2138/am-2022-8643. http://www.minsocam.org/

compositions with an average calculated formula of $(Cu_{0.81}Fe_{0.08}Zn_{0.01}K_{0.01}Ca_{0.01})_{\Sigma 0.92}(Al_{6.05})_{\Sigma 6.05}(P_{1.01}O_4)_4(OH)_{\Sigma 7.13}\cdot 4H_2O$ and $(Cu_{0.82}Fe_{0.07}Zn_{0.01}K_{0.01}Ca_{0.01})_{\Sigma 0.92}(Al_{6.05})_{\Sigma 6.05}(P_{1.03}O_4)_4(OH)_{\Sigma 7.92}\cdot 4H_2O$, respectively. Generally, Trq^{I} displays higher CuO, FeO^{T} and Cr_2O_3 but lower Al_2O_3 and ZnO contents than those of Trq^{II} (Fig. 5). Trq^{I} shows a narrow range of CuO, FeO^{T} and Cr_2O_3 contents of 7.69-8.35 wt%, 0.57-0.74 wt% and 0.11-0.19 wt%, respectively. The Al_2O_3 and ZnO concentrations of Trq^{I} are 37.01 to 37.98 wt% and 0.07 to 0.10 wt%, respectively. The Trq^{I} has A site of 0.88-0.97 apfu that is mainly occupied by Cu (0.78-0.84 apfu) and minor Ba and Ca (up to 0.01). Such invariable compositions of Trq^{I} are consistent with their homogeneity in BSE images (Fig. 4b). In the case of Trq^{II}, compositional differences are determined from the core to rim which show gradually depletion of CuO, FeO and Cr_2O_3 and enrichment of Al_2O_3 and ZnO contents (Fig 5b-f), accompanied by cation deficiency in the A site and increase of H_2O contents (Fig. 6). Correspondingly, the unit formula of Trq^{II} shows a relatively large compositional range of $(Cu_{0.31\text{-}0.82}Fe_{0.03\text{-}0.07}Zn_{0.01\text{-}0.03}K_{0.01\text{-}0.02}Ca_{0.01})_{\Sigma 0.37\text{-}0.93}(Al_{5.92\text{-}6.37})_{\Sigma 5.92\text{-}6.37}(P_{1.03\text{-}1.07}O_4)_4(OH)_{\Sigma 6.84\text{-}7.43}\cdot 4H_2O$.

LA-ICP-MS elemental mapping

As shown in Fig. 7a, two types of turquoise are recognized. Anhedral Trq^{I} has compositional homogeneity and displays higher concentrations of Cu, Fe and Ti, evidenced on trace element maps (Fig. 7b-d). Elemental mapping of Trq^{II} reveals more pronounced laminations of concentric geometry. Both the core and rim of Trq^{II} grain share an enrichment of Zn and U in comparison with Trq^{I} (Fig. 7e, f). The core shows slightly higher Cu, Fe, Ti and Zn concentrations with a decrease trend towards the outer zones. Zhou et al. (2017) interpreted analogous zonation to an environment of changing chemical and/or physical conditions. Noticeably, Trq^{I} and Trq^{II} are overprinted by a thin vein enriched in Sr and La along

276 the turquoise-quartz contact (Fig. 7g, h).

277 **Fluid inclusion data**

278 Fluid inclusions in quartz and barite that coexisted with Trq^{I} and Trq^{II} are identified as fluid
279 inclusion assemblages (FIA) according to their textural characteristics, illustrating groups of coeval
280 inclusions (Goldstein and Reynolds, 1994). Primary inclusions were entrapped on the growing faces of
281 the quartz during its precipitation, and the pseudosecondary inclusions were entrapped in fractures
282 during the growth of the quartz which were commonly overgrown by a layer of the host minerals
283 (Roedder, 1984). Accordingly, isolated fluid inclusions and FIA entrapped along the growing face of the
284 mineral grain are presumed to be most likely primary (Fig. 8a-c). Intra-crystal FIA within the barite and
285 quartz that stop at the grain boundary are assumed to be pseudosecondary (Fig. 8d-f).
286 Microthermometric measurements were conducted on the primary and pseudosecondary inclusions as
287 shown in Table 2. Bulk density of fluid inclusions were calculated using the Flincor software (Brown,
288 1989) and the computer program from Bakker (1997, 2003).

289 Three primary types of fluid inclusions are identified according to the phase relations at room
290 temperature and compositional data revealed by Raman spectroscopic analysis, including:
291 aqueous-carbonic (Type I), carbonic (Type II) and aqueous-salt (Type III) inclusions. Type I inclusions
292 have two phases at room temperature in which the liquid phase consists of C_3H_8, C_2H_6, and H_2O (Fig.
293 9a), whilst the vapor phase, occupying 5-90 percent of the total volume of the inclusion, is composed of
294 CH_4 and N_2 (Table 3; Fig. 9b). The Type I inclusions could be further subdivided into two types on the
295 basis of the degree of filling (F): Type I_a is vapor-rich ($F > 0.6$) and Type I_b is liquid-rich ($F = 0.1$-0.4).
296 They are mainly found in the Qtz^{I}, coexisting with Type II inclusions as fluid inclusion assemblages

297 (FIA) along the growing face of Qtz^{I}, exemplified as a group of primary inclusions trapped coevally
298 (Roedder, 1984; Fig. 8b, c).

299 Accurate estimation of salinities of Type I inclusions is prevented because the melting temperatures
300 of clathrates are no longer a function of salinity as a result of the addition of the CH_4 and N_2 (Jia et al.,
301 2000). Thus, the simplified NaCl-H_2O system may be acceptable for the maximum salinity calculation
302 (Collins, 1979). In Qtz^{I}, Type I_a inclusions have final ice melting temperatures ($T_{m, ice}$) ranging from -6.6
303 to -2.5 °C, corresponding to low salinities of 4.4 to 11.9 wt% NaCl equiv., with calculated densities of
304 0.36-0.58 g/cm^3 (Davis et al., 1990). The total homogenization temperatures (T_h) of the Type I_a
305 inclusions range from 357 to 455 °C. Type I_b inclusions yield lower T_h of 217 to 340 °C and show
306 similar $T_{m, ice}$ of -5.5 to -1.4 °C to those of Type I_a inclusions, equivalent to a salinity of 2.5 to 9.9 wt%
307 NaCl equiv., resulting in the density of 0.68 to 0.95 g/cm^3. Some of Type I inclusions display clathrate
308 melting temperatures ($T_{m, clath}$) of 12 to 17 °C.

309 Type II inclusions are dominant in Qtz^{I} and Brt^{I} as individual or coexisting with Type I inclusions
310 along trails, and their abundances decrease in Qtz^{II}. They are 10 to 20 μm in diameter and composed of a
311 single phase (liquid CH_4-N_2 or vapor CH_4-N_2; Table 3) at room temperature, which develop into
312 two-phase inclusions on cooling to < 90 °C. Estimations of initial ice melting temperatures (T_m) failed
313 because phase changes were invisible below -120 °C. Generally, they homogenized into the liquid phase
314 at temperatures between -145 and -127 °C and partly into vapor phase at -144 to -136 °C, which are
315 much lower than the critical point of pure CH_4 (-82.6 °C), suggesting the addition of dissolved N_2, which
316 is also evidenced by laser Raman analysis (Fig. 9c).

317 Type III inclusions mainly occur in Qtz^{II}, Brt^{II} and Brt^{I} as isolated two-phase inclusions or
318 randomly coexisting with Type II inclusions, consisting of 5-25 vol% vapor and 75-95 vol% liquid.

Raman spectra of vapor and liquid phases from Type III inclusions show narrower and more symmetrical bands (Fig. 9d) than those from the pure water showing relatively broad signal, with a shoulder situated in lower wavenumbers, indicating the addition of salts (Lawler and Crawford, 1983; Mernagh and Wilde, 1989). Moreover, measurements of initial ice melting temperatures (T_m) for Type III inclusions are -24.2 to -21.3 °C, implying the NaCl is dominant among the dissolved salts (Davis et al., 1990). Based on the equations of Davis et al. (1990), aqueous fluids of Qtz^{II} show relatively broad range of 1.6-9.3 wt.% NaCl equiv., whereas those from Brt^{I} and Brt^{II} fall into 1.2-4.1 and 1.8-6.6 wt.% NaCl equiv., respectively (Table 2). Type III inclusions in Brt^{I}, Qtz^{II} and Brt^{II} homogenized into the liquid phase at temperatures of 195-355 °C, 136-315 °C and 222-341 °C (Table 2). As shown in the Fig. 10c and g, the T_h of the Type III inclusions follow the unimodal distributions and decrease in the order of the Brt^{I}, Qtz^{II} and Brt^{II}, displaying the mean values of 292 ± 43 °C, 239 ± 40 °C and 238 ± 11 °C, respectively. From the estimations of T_h and salinity, the bulk density of Type III fluid inclusions in Brt^{I}, Qtz^{II} and Brt^{II} are calculated as 0.60-0.81 g/cm^3, 0.78-0.91 g/cm^3 and 0.62-0.86 g/cm^3, respectively.

Since the homogenization temperatures of fluid inclusions may not represent the actual trapping temperatures for the fluids, pressure correction is conducted followed the iterative method of Roedder (1984) and Fan et al. (2003). Isochores are obtained for the Type I_b CH_4-NaCl-H_2O inclusions and Type III NaCl-H_2O inclusions to constrain the pressure and temperature of the fluids, using Flincor software and the computer program of Bakker (2003) (Shepherd, 1986; Brown, 1989). For Type I_b CH_4-NaCl-H_2O inclusions in the Qtz^{I}, the homogenization temperatures are 217 °C to 340 °C. The preliminary pressure is about 150 MPa from Fig. 11. Accordingly, the pressure correction at 150 MPa is about +130 °C (Roedder, 1984). Therefore, the trapping temperature for Type I_b inclusions is from 347 °C to 470 °C and the recalculated trapping pressure from Fig. 11 is greater than 300 MPa.

This is the peer-reviewed, final accepted version for American Mineralogist, published by the Mineralogical Society of America.
The published version is subject to change. Cite as Authors (Year) Title. American Mineralogist, in press.
DOI: https://doi.org/10.2138/am-2022-8643. http://www.minsocam.org/

For Type III NaCl-H_2O inclusions in the Brt^I, Qtz^{II} and Brt^{II}, the analyzed homogenization temperatures are 195-355°C, 136-315 °C and 222-341 °C, corresponding to the low minimum pressure estimations of 50-150 MPa from Fig. 11. At such pressure, the corresponding temperature correction would be +130 °C in Brt^I and +50 °C in Qtz^{II} and Brt^{II} (Roedder, 1984). Thus, estimated entrapping temperatures for Type III inclusions in Brt^I, Qtz^{II} and Brt^{II} are 325-485 °C, 186 -365 °C and 272-391 °C, and the recalculated trapping pressure is 150-250 MPa.

H-O-C isotope data

Hydrogen, oxygen and carbon isotope data were determined and listed in Table 4. The measured $\delta^{18}O$ values of Qtz^I range from 20.9 to 22.4 ‰, and that of Qtz^{II} is 22.6 ‰. Hydrothermal fluids in equilibrium with Qtz^I have the calculated oxygen isotopic compositions of 17.3 to 18.8 ‰, using the quartz-water fractionation equation of Clayton et al. (1972) and the average pressure-corrected homogenization temperature of 422 °C. Calculated oxygen isotopic composition of hydrothermal fluids equilibrated with Qtz^{II} is relatively lower at 15.0 ‰ on the basis of the lower pressure-corrected homogenization temperature of 282 °C. The measured δD values of fluid inclusions in Qtz^I and Qtz^{II} are extremely negative and range from -111 to -93 ‰. Measured $\delta^{13}C$ values of CO_2 and CH_4 in quartz fluid inclusions range from -27.6 to -22.5 ‰ and -40.8 to -30.3 ‰, respectively.

DISCUSSION

Mineralogy of the turquoise occurrence

On the basis of SEM-BSE images and EPMA data, two types of gemstone turquoise could be distinguished: Trq^I and Trq^{II}. Trq^I appears homogeneous in SEM-BSE images, mainly comprises of turquoise endmember as shown by relatively high Cu (apfu) at A site (up to 0.84 apfu), low A-site

This is the peer-reviewed, final accepted version for American Mineralogist, published by the Mineralogical Society of America.
The published version is subject to change. Cite as Authors (Year) Title. American Mineralogist, in press.
DOI: https://doi.org/10.2138/am-2022-8643. http://www.minsocam.org/

vacancy and calculated water content (Table 1; Foord and Taggart, 1998). Trq^{II} with oscillatory zoning texture consists of turquoise endmember at the core and gradually evolves to the planerite endmember towards the rim as a result of the decreasing A site occupancy, accompanied by increasing water content (Fig. 6; Rossi et al., 2017; Jomeh et al., 2020). Of note, Trq^{II} contains anomalous concentrations of Cr, Zn, U, Pb and Sr, which are obviously discriminated from those of Trq^{I}. Such compositional and textual distinctions could be explained by different properties of non-magmatic hydrothermal fluids and changing physicochemical conditions when Trq^{I} and Trq^{II} precipitated.

Source and evolution of mineralizing fluids

Microthermometric data combined with laser Raman spectroscopic analysis reveal that there are three types of fluid inclusions in the quartz and barite associated with the formation of Trq^{I} and Trq^{II}: the carbonic-aqueous fluid inclusion (Type I), pure CH_4-N_2 fluid inclusion (Type II), and the aqueous-salt fluid inclusion (Type III), from which the presence of pure CH_4-N_2 fluids is significantly distinct from the meteoric water that is represented by the H_2O-CO_2-NaCl system (Jenkin et al., 1994; Menzies et al., 2014).

Coexistences of pure CH_4-N_2 inclusions (type II) and carbonic-aqueous inclusions (type I) within trails along the quartz growth zones form distinct primary FIA in the Qtz^{I} (Fig. 8b, c), reflecting they were trapped coevally (Roedder, 1984). Of particular note is that Type I_a and I_b inclusions with various ratios of vapor to liquid display a large range of homogenization temperatures to both vapor and liquid (Fig. 8c and 10c), which could be ascribed to various molar volumes of inclusions due to the randomly mixtures of two phases in fluids resulted from the heterogeneous trapping of the immiscible fluids (Ramboz et al., 1982). The Type II fluid inclusions represent the pure CH_4-N_2 fluids, and the Type I_a and

This is the peer-reviewed, final accepted version for American Mineralogist, published by the Mineralogical Society of America.
The published version is subject to change. Cite as Authors (Year) Title. American Mineralogist, in press.
DOI: https://doi.org/10.2138/am-2022-8643. http://www.minsocam.org/

383 I_b fluid inclusions with various V/L ratios reflect the heterogeneous trapping of the aqueous fluids and
384 pure CH_4-N_2 fluids. The coexistence of such three types of fluid inclusions is the most direct evidence of
385 fluid immiscibility in which CH_4-N_2 might be exsolved from aqueous fluids due to the low CH_4-N_2
386 solubility limits (Ramboz et al., 1982; Xu, 1998; Chi et al., 2021). For such case, Type I_a inclusions with
387 higher vapor volumes commonly homogenize at temperatures far above the actual trapping temperatures,
388 which are supposed to be geologically meaningless. Hence, Type I_b inclusions with the lowest V/L ratios
389 are thought to most likely represent the primary free liquid, and their molar volumes and
390 homogenization temperature are taken to be the best estimations of those of the original liquid (Roedder,
391 1984).

392 In summary, the earlier turquoise-forming fluids contain all of three types of fluids, while later ones
393 were primarily aqueous fluids with smaller CH_4-N_2 components, promoting higher salinity with less
394 proportions of CH_4 and N_2 (Fig. 12a, b). Non-magmatic hydrothermal fluids in Qtz^I and Brt^I associated
395 with Trq^I were characterized by relatively high proportions of CH_4 and N_2, low salinities of 1.2-9.9 wt.%
396 NaCl equiv. with most values lying between 6-8 wt.% NaCl equiv., and fairly high homogeneous
397 temperature (T_h) of 325-485 °C (Table 2; Fig. 12a-c). On the contrary, the fluids responsible for the
398 formation of Qtz^{II} and Brt^{II} coexisting with Trq^{II} are devoid of CH_4 and N_2, but show similar salinities of
399 1.6-9.3 and 1.8-6.6 wt.% NaCl equiv. and lower average T_h of 289 ± 40 °C and 288 ± 11 °C,
400 respectively (Table. 2; Fig. 12a, b and d). In either case, the homogenization temperatures of the fluid
401 inclusions are pronouncedly higher than those of the meteoric waters ranging from 17 to 35 °C (Shi and
402 Cai, 2011), implying a much more differentiated source.

403 The main stage of fluid immiscibility events mainly occurred during the formation of the
404 homogeneous Trq^I (Fig. 12c). The immiscible fluids of two endmembers, namely pure CH_4-N_2 fluids

This is the peer-reviewed, final accepted version for American Mineralogist, published by the Mineralogical Society of America.
The published version is subject to change. Cite as Authors (Year) Title. American Mineralogist, in press.
DOI: https://doi.org/10.2138/am-2022-8643. http://www.minsocam.org/

and aqueous fluids, have been rarely documented in the context of gem turquoise mineralization. Cox et al. (1995), Jia et al. (2000) and Fu et al. (2014) have attributed the presence of CH_4 to the interaction of magmatic and/or metamorphic fluids with carbonaceous slates during the metamorphism. As for the production of N_2 in fluids, previous studies confirmed that the release of NH_3 from wall rocks is a significant source of nitrogen following the equation at 600 K and 1.8 kbar (Bottrell and Miller, 1990; Shepherd et al., 1991; Andersen et al., 1993; Berwick et al., 2007):

$$3C+4NH_3 = 3CH_4 + 2N_2 \quad (3)$$

Therefore, we speculate that the methane and nitrogen were leached into fluids as a consequence of extensive fluid-rock interaction.

This hypothesis is also confirmed by the stable isotopic compositions. Turquoise-forming fluids in equilibrium with quartz have $\delta^{18}O$ values of 15.0-18.8 ‰, showing a great affinity to those of metamorphic water (Fig. 13a; Taylor, 1974). Also, the absence of simultaneous magmatic activity in the study area precludes a magmatic origin for the fluids (Fig. 1; Zhang et al., 2019). Consequently, it is suggested that the turquoise-forming fluids are mainly metamorphic fluids.

Sedimentary rocks are generally composed of hydrous phyllosilicates, quartz, feldspars, carbonates and organic matter. Increasing temperature and pressure during prograde metamorphism will lead to the dehydration and decarbonation of the metasedimentary rocks, thus defining the nature of coexisting metamorphic fluids (Yardley, 1989; Ague, 2003; Stepanov, 2021). Besides, semi-quantitative calculation suggested that the devolatilization of a rock pile could form 2-5 wt.% aqueous fluids around the greenschist to amphibolite facies transition, indicative of a large volume of fluids (Phillips and Powell, 2010). Therefore, evidence above permits the quartz veins to be an end product of metamorphic devolatilization. Breakdown of chlorite, probably derived from the schist in the Lower Cambrian

427 Shuigoukou Formation (Zhao et al., 2017; Zhang et al., 2019), likely accounted for the generation of
428 metamorphic fluids during the regional low greenschist facies metamorphism in the turquoise deposit
429 following the reaction (Bebout and Fogel, 1992; Wang et al., 2019):

430 2 Phengite + Chlorite = Muscovite + Biotite + Quartz + $4H_2O$ (4)

431 Such fluids, mainly distributed in situ at the grain-scale level throughout the rock, further
432 promote the reactions with rocks and minerals, which eventually lead to the enrichment of elements in
433 the fluids (Stepanov, 2021). With regard to the fluid compositions, they depend predominantly on the
434 primary mineralogy of the source rocks (Yardley and Graham, 2002). The lack of minerals containing
435 chlorine in the slates leads to the low salinity of the turquoise-forming metamorphic fluids.

436 Notably, the metamorphic fluids are characterized by significantly depleted δD values similar to
437 those from waters that have reacted with organic matter (Fig. 13a; Taylor, 1974; Sheppard, 1986). The
438 oxidation of CH_4 into CO_2 due to increasing fO_2 could dramatically deplete deuterium in fluids (Fu et al.,
439 1991; Tarantola et al., 2007), while an increase of CO_2 contents is not observed in metamorphic fluids
440 by microthermometry. Thus, possible interpretation of such low δD values might be the interaction
441 between metamorphic fluids and organic materials (Kesler et al., 1997). Carbon isotope data are also
442 useful for the determination of the potential sources in ore deposits (Fig. 13b; Hu et al., 2021; Ma et al.,
443 2021; Niu et al., 2022): a marine carbonate source with $\delta^{13}C$ values of 0 ‰; an organic matter source
444 with $\delta^{13}C$ value from -35 ‰ to -15 ‰ and a magmatic source with $\delta^{13}C$ values of -9 ‰ to -3 ‰. The
445 carbon isotope compositions of CO_2 in the turquoise-forming system display obviously sedimentary
446 organic carbon characteristics (-27.6 to -22.5 ‰; Fig. 13b). During the oxidation or hydrolysis of
447 organic matter (i.e., graphite) at the temperature around 500 ºC, strong carbon isotope fractionation
448 occurs between the released gaseous CO_2 phase and the source rocks. The former prefers to be enriched

449 in ^{13}C, leading to an increase of the $\delta^{13}C$ values by almost +10 ‰ than those of the source rocks
450 (Bottinga, 1968). Thus, the $\delta^{13}C$ values of potential source rocks for the gaseous CO_2 are likely more
451 negative as the measured $\delta^{13}C_{CO2}$ values from fluid inclusions and cover the range of the reported bulk
452 carbon isotope compositions of the Lower Cambrian Shuigoukou Formation (-35 ‰ to -15 ‰; Hou,
453 2008). Moreover, the measured $\delta^{13}C$ values of methane from fluid inclusions between -40.8 ‰ and
454 -30.3 ‰ are typically consistent with those produced by primary cracking of kerogen within the range of
455 -45 ‰ to -31 ‰ (Schoell, 1980; Lueders et al., 2012). All these observations described above imply CO_2
456 and CH_4 in the turquoise-forming fluids were predominantly derived from the organic carbon coming
457 from the carbonaceous slates by fluid-rock interaction.

458 Such unusual characteristics of C-H-O isotope compositions have been widely recognized
459 regarding the formation of Pb-Zn-Mo-Au deposits, illustrating the interaction between ore-forming
460 fluids and organic matter in the host rocks (e.g., Kelser et al., 1997; Xia et al., 2013; Zhou et al., 2015;
461 Ma et al., 2021; Niu et al., 2022). Low δD values of fluid inclusions have been reported by Kelser et al.
462 (1997) in the Mississippi Valley type (MVT)-forming brines, of which hydrogen and oxygen isotopes of
463 fluids plot along the meteoric water line with $\delta^{18}O$ and δD values of 2 ‰ and -41 ‰ and then evolved to
464 the very low δD values of -87 ‰. Combined with the depleted $\delta^{13}C$ values of CH_4 of inclusions, the
465 mineralizing brines in the MVT deposits were identified as seawater that was modified by interaction
466 with organic matter in the host rocks. Moreover, Niu et al. (2022) interpreted H-O isotope compositions
467 of ore-forming fluids ranging from -111.2 ‰ to -85.5 ‰ and +9.0 ‰ to +11.5 ‰ as mixtures of
468 magmatic fluids with the organic-containing water in the Suixian Mo deposit. The presence of CH_4 and
469 the depleted $\delta^{13}C$ values of CO_2 in the fluid inclusions also pointed to the thermochemical reaction
470 between the magmatic fluids and organic matter from hosted metamorphic rocks.

In this regard, fluid evolution could be reconstructed for the turquoise deposit in Zhushan County. The turquoise-forming fluid system in the Zhushan County was initially CH_4-N_2-rich, high temperature (325-485 °C), low salinity (1.2-9.9 wt.% NaCl equiv.), and had low CO_2/CH_4 ratios, coexisting with immiscible CH_4-N_2 fluids. With decreasing temperature (186-391°C), fluids progressively evolved to become CH_4-N_2-poor, with lower salinity (1.6-6.6 wt.% NaCl equiv.) (Fig. 12). Throughout this process, metamorphic fluids locally interacted with organic matter from wall rocks, modifying fluid C-H-O isotope compositions.

The source of metals

Previous studies proposed that the turquoise deposits were sourced from the Lower Cambrian Shuigoukou Formation by weathering and leaching of the low-temperature oxidized surface water in a supergene environment (Tu et al., 1996, 1997; Qin et al., 2015; Liu et al., 2020). We agree with the general view that the turquoise-forming elements were sourced from the Cambrian carbonaceous slates. However, as discussed above, the Zhushan turquoise displays characteristics best explained by derivation from metamorphic fluids: high temperature, high contents of CH_4 and N_2, and H-O isotopic compositions distinct from meteoric water. Considering the above-mentioned features, the following discussion will concentrate on the essential origin of Cu, Fe, P and Al to form turquoise.

According to the previous geochemical analysis of the Shuigoukou Formation, the black slates contain appreciable amounts of Cu in the range of 10-1907 ppm (Wang, 2009; You et al., 2018), supporting the source bed for the turquoise mineralization. SEM results illustrate that the slate mainly consists of quartz, apatite, barite, muscovite, magnetite and pyrite with minor amounts of monazite, rutile and xenotime. Electron probe micro-analysis (EPMA) and X-ray diffraction (XRD) analysis have

492 also been carried out by Wang (2016), You et al. (2018) and Liu et al. (2021), which further refined the
493 mineralogy of the carbonaceous slates with the presence of clay minerals including kaolinite and illite,
494 and non-clay mineral assemblages of chalcopyrite, feldspar, calcite, dolomite and siderite in wall rocks.

495 As has been noted, minerals above are randomly dispersed in the carbonaceous slates, thus
496 insufficient enriching Cu, Fe, Al and P to the economic value in the absence of remobilization as a result
497 of weathering-leaching process, igneous intrusion, or metamorphic activity (Chen et al., 1990; Wang,
498 2009). Turquoise mixed with goethite, alunite, and jarosite in veins hosted in a shale unit have been
499 attributed to a supergene origin at low temperatures (Crook and Lueth, 2014). Previous studies
500 elucidated the oxidizing acid aqueous fluid, formed by the oxidation of pyrite and transformation of clay
501 minerals in supergene environments, could promote the chemical reactions and ore metal transportations
502 which further facilitated the formation of the turquoise (Crook and Lueth, 2014; Li et al., 2022).
503 Nevertheless, the absence of oxidized minerals such as malachite and hematite, coexistence of turquoise
504 with quartz and barite, and high CH_4/CO_2 ratios in fluids of Zhushan turquoise preclude a supergene
505 environment of formation. Moreover, no magmatic activity has been observed in the region (Fig. 1;
506 Zhang et al., 2019). Therefore, we argue that metamorphic fluids generated from the dehydration and
507 devolatilization of the carbonaceous slates produced the quartz-barite veins that deformed
508 synchronously with wall rocks (Fig. 2, 4; Wang, 2009). In this process, we suggest that Cu, Fe, Ba, U, Ti,
509 Al and P were remobilized from apatite, feldspar, barite, muscovite, chalcopyrite, magnetite, pyrite,
510 rutile, monazite and xenotime in the slates during water-rock interaction, and transferred into fluids as
511 chloride complexes in the function of the saline metamorphic fluids, ultimately to precipitate as gem
512 turquoise in tectonically favorable sites (Chen et al., 1990; Yardley and Graham, 2002).

513 We interpret the compositional changes from turquoise (Trq^I) to turquoise-planerite solid solution

This is the peer-reviewed, final accepted version for American Mineralogist, published by the Mineralogical Society of America.
The published version is subject to change. Cite as Authors (Year) Title. American Mineralogist, in press.
DOI: https://doi.org/10.2138/am-2022-8643. http://www.minsocam.org/

514 (Trq^{II}) reflect evolution of the metamorphic fluids during the process of fluid-rock interaction. The
515 fluid-rock interaction process was recorded by the evolution of fluid inclusions throughout the different
516 stages. Legros et al. (2020) argued that the primary fluids from the intrusion in the Cantung tungsten
517 deposit are CO_2-rich which indicate their primary magmatic source, while fluids that interacted intensely
518 with the surrounding limestone are CH_4-rich. Correspondingly, carbonic-aqueous fluids with immiscible
519 CH_4-N_2 fluids in Trq^{I}-related samples (Fig. 12c) likely represent the initial fluids that underwent
520 extensive interaction with surrounding carbonaceous slates, increasing the turquoise-forming elements
521 in water. In contrast, the fluids related to the Trq^{II} are CH_4-N_2-poor (Fig. 12d) and suggest the decreasing
522 reactivity of fluids with the wall rocks, inducing the decrease of necessary metals for the turquoise
523 (Table 1; Fig. 8).

524 Alternatively, such a pattern might be explained by the changing elemental partition behaviors
525 during the precipitation of the turquoise. The uncertainties regarding fluid-rock and fluid-turquoise
526 partitioning hinder the understanding of this mechanism. According to Skora et al. (2006), the decrease
527 of Cu and Fe contents in the oscillatory zoning Trq^{II} could also be interpretated by the transient matrix
528 diffusion model that the Trq^{II} have crystallized in the depleted matrix where Cu, Fe and other elements
529 uptake were restricted by diffusion in the matrix surrounding the crystals. Nevertheless, neither
530 explanation could account for the significantly decreasing CH_4-N_2 contents in the Trq^{II}-forming fluids.
531 Thus, we favor our interpretation that the decline of interaction between metamorphic fluid and
532 metasedimentary rocks drove the geochemical evolution from homogeneous turquoise in Trq^{I} towards
533 turquoise-planerite solid solution in Trq^{II}.

534 Another possible metal source (Cu, Fe, V, Zn and U) is envisioned on the basis of large amount of
535 organic carbon in the Shuigoukou Formation, as indicated by the high total organic carbon (TOC)

content ranging from 0.46 to 2.43 % (Wang, 2009; You et al., 2018). Previous organic geochemical studies have confirmed there is a certain positive correlation between the metal contents (V, Ni, Zn, Cu, Os, Rh, Pt, Pd, Ir, Ru, Ag and U) and the total organic carbon content (TOC) in the Lower Cambrian Shuigoukou Formation (You et al. 2018). Such correlations have been reported in other carbonaceous rock-hosted Au-V-U ore deposits (Hu et al., 2000; Hou, 2008; Wang, 2009; Wang, 2016). Metals could be absorbed on organic matter before generating primary sulfides by the action of H_2S under reducing conditions (Chen et al., 1990). Moreover, experimental studies proved that gold-metallogenic elements could strongly combine with immature and low-maturity organic matter due to the action of chelation (Hu et al., 1993). Thus, organic-rich carbonaceous formations are supposed to highly promote the primary accumulation of metallogenic elements as the metal sources.

We interpret that the evolution of organic matter in the carbonaceous slates could facilitate the migration of metals in the aqueous fluids. Decomposition of organic matter would lead to the transformation from the organic carbon into gaseous H_2O, N_2, H_2S and hydrocarbon compounds (e.g., CH4) which could self-extract metals or combine with metals as metal-organic complexes, promoting the release of metals from slates into fluids and their transportation in aqueous fluids (Breit and Wanty, 1991; Wang, 2009; Wang, 2016). Moreover, degradation and oxidation of organic matter could produce the organic acids, which are mainly composed of the negatively charged hydroxyl group, carboxy group and other function groups. Such groups have been assumed to significantly enhance the combination, adsorption and chelation of the metal ions, allowing soluble metals to migrate over long distances in aqueous fluids (Leventhal and Giordano, 1997; Hu et al., 2000; Qin and Zhou, 2009; Wang, 2009). Metal complexes will then break down from the metamorphic fluids owing to changes in pressure, temperature, and acidity in fluids, resulting in the formation of gem turquoise.

IMPLICATIONS

The turquoise deposit in Zhushan County, western Hubei Province, China, consists of turquoise-quartz-barite veins occurring along or cutting the beddings of the carbonaceous slates. New fluid inclusion and stable isotope data, combined with geological and geochemical evidence, substantiate a new genetic model for gem turquoise worldwide, termed the metamorphic quartz-vein type turquoise deposit. Devolatilization of Lower Cambrian carbonaceous slates transpired during regional metamorphism and deformation, and generated turquoise-forming metamorphic fluids characterized by low salinities (6-8 wt.% NaCl equiv.) at moderate to high temperatures (up to 450 °C). Further support for this model comes from the $\delta^{18}O$ values of turquoise-forming fluids (20.9-22.6 ‰), which are consistent with metamorphic fluids. The presence of CH_4-N_2 fluid inclusions, the remarkably depleted $\delta^{13}C$ values of CO_2 and CH_4 in fluid inclusions from quartz (-27.6 to -22.5 ‰ and -40.8 to -30.3 ‰) and the extremely low δD values of turquoise-forming fluids (-111 to -93 ‰), suggest the intense interaction between the metamorphic fluids and the carbonaceous siliceous slates, leading to immiscibility between pure CH_4-N_2 and carbonic-aqueous fluids during the formation of the homogeneous turquoise. As temperature and reactivity with wall rocks decreased, so did the CH_4 and N_2 contents of fluids. Concurrently, the A site deficiency in the turquoise group minerals became more dominant, leading to the transition from gem turquoise to Cu-bearing planerite solid solutions. Turquoise-forming metals (e.g., Cu, Fe, Ba, U, Ti, Al and P) are assumed to be sourced from the dissolving of various minerals (e.g., apatite, feldspar, barite, muscovite, chalcopyrite, magnetite, pyrite, rutile, monazite and xenotime) in the carbonaceous slates caused by the fluid-rock interaction. Moreover, decomposition of the organic carbon from the Shuigoukou carbonaceous slates might also contribute to the extraction and the transportation of the metals responsible for the formation of turquoise.

ACKNOWLEDGEMENTS

We appreciated Associate Prof. Huimin Su and all members of the LA-ICP-MS lab in the Collaborative Innovation Center for Exploration of Strategic Mineral Resources for their assistance with the trace elemental mapping. No.8th Geological Team of Hubei Geological Bureau is thanked for guide the field trip. We are grateful to Dr. Suo-Fei Xiong, De-Liang Liu, Ying Ma, Zhenpeng Duan, Haoxiang Zhang for their kind help with the analysis. We thank Prof. Paul Tomascak, Dr. Tomasz Powolny and an anonymous reviewer for valuable comments that assisted us to improve this contribution.

FUNDING

This study was financially supported by projects from the National Key R&D Program of China (no. 2022YFC2903504), the National Natural Science Foundation of China (No. 42030811), the No.8th Geological Team of Hubei Geological Bureau, and the State Key Laboratory of Geological Processes and Mineral Resources, China University of Geosciences (No. MSFGPMR03-2)

REFERENCES CITED

Abdu, Y.A., Hull, S.K., Fayek, M., and Hawthorne, F.C. (2011) The turquoise-chalcosiderite Cu(Al, Fe^{3+})$_6$(PO$_4$)$_4$(OH)$_8$·4H$_2$O solid-solution series: A Mossbauer spectroscopy, XRD, EMPA, and FTIR study. American Mineralogist, 96(10), 1433–1442.

Ague, J.J. (2003) Fluid flow in the deep crust. Treatise on Geochemistry, 3, 195-228.

Andersen, T., Austrheim, H., Burke, E.A.J., and Elvevold, S. (1993) N_2 and CO_2 in deep crustal fluids: evidence from the Caledonides of Norway. Chemical Geology, 108, 113–132.

Bakker, R.J. (1997) Clathrates: Computer programs to calculate fluid inclusion V-X properties using clathrate melting temperatures. Computers & Geosciences, 23, 1–18.

Bakker, R.J. (2003) Package FLUIDS 1. Computer programs for analysis of fluid inclusion data and for

603 modelling bulk fluid properties. Chemical Geology, 194, 3-23.

604 Bebout, G.E., and Fogel, M.L. (1992) Nitrogen-isotope compositions of metasedimentary rocks in the
605 Catalina Schist, California: Implications for metamorphic devolatilization history. Geochimica et
606 Cosmochimica Acta, 56, 2839-2849.

607 Bottinga, Y. (1968) Calculation of fractionation factors for carbon and oxygen exchange in the system,
608 calcite-carbon dioxide-water. Journal of Physical Chemistry, 72, 800-808.

609 Breit, G.N., and Wanty, R.B. (1991) Vanadium accumulation in carbonaceous rocks: a review of
610 geochemical controls during deposition and diagenesis. Chemical Geology, 1991, 91(2): 83-97.

611 Bernardino, N.D., Izumi, C.M.S., and de Faria, D.L.A. (2016) Fake turquoises investigated by Raman
612 microscopy. Forensic science international, 262, 196-200.

613 Berwick, L., Greenwood, P., Kagi, R., and Croue, J.P. (2007) Thermal release of nitrogen organics from
614 natural organic matter using micro scale sealed vessel pyrolysis. Organic Geochemistry, 38, 1073–
615 1090.

616 Bottrell, S.H., and Miller, M.F. (1990) The geochemical behavior of nitrogen compounds during the
617 formation of black shale hosted quartz-vein gold deposits, North Wales. Applied Geochemistry, 5,
618 289–296.

619 Brown, P.E. (1989) FLINCOR: a microcomputer program for the reduction and investigation of
620 fluid-inclusion data. American Mineralogist, 74, 1390-1393.

621 Brunsgaard-Hansen, S., Berg, R.W., and Stenby, E.H. (2002) How to determine the pressure of a
622 methane-containing gas mixture by means of two weak Raman bands, v3 and 2v2. Journal of
623 Raman Spectroscopy, 33, 160–164.

624 Burke, E.A.J. (2001) Raman microspectrometry of fluid inclusions. Lithos, 55, 139–158.

625 Cejka, J., Sejkora, J., Macek, I., Malikova, R., Wang, L.N, Scholz, R., Xi, Y.F., and Frost, R.L. (2015)
626 Raman and infrared spectroscopic study of turquoise minerals. Spectrochimica Acta Part A:
627 Molecular and Biomolecular Spectroscopy, 149, 173-182.

628 Chen, N.S., Yang, X.Z., Liu, D.H., Xiao, X.J., Fan, D.L., and Wang, L.F. (1990) Lower Cambrian black
629 rock series and associated stratiform deposits in Southern China. Chinese Journal of Geochemistry,
630 8(2), 244-255.

631 Chen, Q.L., Yin, Z.W., Qi, L.J., and Xiong, Y. (2012) Turquoise from Zhushan County, Hubei Province,

China. Gems & Gemology, 48(3), 198–204.

Chen, Y.J., Zhai, M.G., and Jiang, S.Y. (2009) Significant achievements and open issues in study of orogenesis and metallogenesis surrounding the North China continent. Acta Petrologica Sinica, 25, 2695–2726 (in Chinese with English abstract).

Chi, G.X., Diamond, L.W., Lu, H.Z., Lai, J.Q., and Chu, H.X. (2021) Common Problems and Pitfalls in Fluid Inclusion Study: A Review and Discussion. Minerals, 11, 1-17.

Clayton, R.N., O'Neil, J.L., and Meyeda, T.K. (1972) Oxygen isotope exchange between quartz and water. Journal of Geophysical Research, 77, 3057–3067.

Clayton, W.M., and Mayeda, T.K. (1963) The use of bromine pent a fluoride in the extraction of oxygen from oxides and silicates for isotopic analysis. Geochimica et Cosmochimica Acta, 27, 43–52.

Collins, P.L.F. (1979) Gas hydrates in CO_2-bearing fluid inclusions and the use of freezing data for estimation of salinity. Economic Geology, 74, 1435–1444.

Cox, S.F., Sun, S.S., Etheridge, M.A., Wall, V.J., and Potter, T.F. (1995) Structural and geochemical controls on the development of turbidite-hosted gold quartz vein deposits, Wattle Gully mine, central Victoria, Australia. Economic Geology, 90, 1722–1746.

Crook, J.C. and Lueth, V.W. (2014) A geological and geochemical study of a sedimentary-hosted turquoise deposit at the Iron Mask mine, Orogrande, New Mexico, in: Geology of the Sacramento Mountains region. New Mexico Geological Society, Guidebook, 65th Field Conference, p. 227-233.

Davis, D.W., Lowenstein, T.K., and Spencer, R.J. (1990) Melting behavior of fluid inclusions in laboratory-grown halite crystals in the systems NaCl–H_2O, NaCl–KCl–H_2O, NaCl–$MgCl_2$–H_2O, and NaCl– $CaCl_2$–H_2O. Geochimica et Cosmochimica Acta, 54, 591–601.

Disbrow, A.E., and Stoll, W. C. (1957) Geology of the Cerrillos Area, Santa Fe County, New Mexico, 48, p. 73. State Bureau of Mines and Mineral Resources, New Mexico Institute of Mining & Technology.

Dumanska-Slowik, M., Weselucha-Birczynska, A., Natkaniec-Nowak, L., Gawel, A., Wlodek, A., and Kulmaczewska, K. (2020) Blue or green? Turquoise–planerite species from Carico Lake Valley in Nevada, the United States: Evidence from Raman spectroscopy. Journal of Raman Spectroscopy, 51, 346–356.

Fan, H.R., Zhai, M.G., Xie, Y.H., and Yang, J.H. (2003) Ore-forming fluids associated with granite

hosted gold mineralization at the Sanshandao deposit, Jiaodong gold province, China. Mineralium Deposita, 38, 739–750.

Foord, E.E., and Taggart, J.E. (1998) A reexamination of the turquoise group: the mineral aheylite, planerite (redefined), turquoise and coeruleolactite. Mineralogical Magazine, 62(1), 93–111.

Fritsch, E., Mcclure, S.F., Ostrooumov, M., Andres, Y., and Kammerling, R.C. (1999) The identification of Zachery-treated turquoise. Gems & Gemology, 35(1), 4-16.

Fu, B., Mernagh, T.P., Fairmaid, A.M., Phillips, D., and Kendrik, M.A. (2014) CH_4-N_2 in the Maldon gold deposit, central Victoria, Australia. Ore Geology Reviews, 58, 225-237.

Fu, M., Changkakoti, A., Krouse, H.R., Gray, J., and Kwak, T.A.P. (1991) An oxygen, hydrogen, sulfur, and carbon isotope study of carbonate-replacement (skarn) tin deposits of the Dachang Tin Field, China. Economic Geology, 86(8), 1683-1703.

Goldstein, R.H., and Reynolds, T.J. (1994) Systematics of Fluid Inclusions in Diagenetic Minerals, 31, 199 p. Society for Sedimentary Geology SEPM Short Course.

Hedenquist, J.W., and Lowenstern, J.B. (1994) The role of magmas in the formation of hydrothermal ore deposits. Nature, 370, 495–510.

Herzberg, G. (1950) Molecular Spectra and Molecular Structure I. Spectra of Diatomic Molecules, Second edition. Van Nostrand, Princeton, NJ. 658 p.

Hou, J.F. (2008) Metallogenetic characteristics and regularities of Au-V mineralization in Lower Cambrian black rock series, Southern Qinling Mountain, China, 87 p. M.D. thesis, Northwest University (in Chinese with English abstract).

Hu, D.L., Jiang, S.Y., Duan, D.F., and Xiong, S.F. (2021) Fluid origin and evolution of the Ruanjiawan W-Cu-(Mo) deposit from the Edong District in the Middle-Lower Yangtze River metallogenic belt of China: Constraints from fluid inclusions and H-O-C-S isotopes. Ore Geology Reviews, 139, 104428.

Hu, K., Liu, Y.J., and Jia, R.F. (1993) Experimental study of gold accumulation by organic matter under low-temperature hydrothemical conditions. Science in China (Series B), 23(8), 880 (in Chinese).

Hu, K., Zhai, J.P., Liu, Y.J., Wang, H.N., Zhang, J.R., and Jia, R.F. (2000) Genesis and organic geochemical characteristics of the carbonaceous rock stratabound gold deposits, South China. Science in China (Series D: Earth Science), 5, 507-520.

690 Hu, J.M., Meng, Q.R., Bai, W.M., and Zhao, G.C. (2002) Mid-Late Palaeozoic extension of the Wudang
691 block in the South Qinling tectonic belt, China. Geological Bulletin of China, 21, 471–477 (in
692 Chinese).
693 Jenkin, G.R.T., Craw, D., and Fallick, A.E. (1994) Stable isotopic and fluid inclusion evidence for
694 meteoric fluid penetration into an active mountain belt; Alpine Schist, New Zealand. Journal of
695 Metamorphic Geology, 12, 439-444.
696 Jia, Y.F., Li, X., and Kerrich, R. (2000) A fluid inclusion study of Au-bearing quartz vein systems in the
697 Central and North Deborah deposits of the Bendigo Gold Field, central Victoria. Australia.
698 Economic Geology, 95, 467–496.
699 Jiang, Z.C., Chen, D.M., Wang, F.Y., Li, W.Y., Cao, X.Q., and Wu, Q.X. (1983) Thermal properties of
700 turquoise and its intergrowing minerals in a certain district of China. Acta Mineralogica Sinica,
701 3(3), 198-206 (in Chinese).
702 Jin, G.S., Liu, H.B., Zhang, J.F., Han, J., Qiu, L.F., Li, J.J., Zhang, J., and Shi, X. (2021) On-line
703 continuous flow analysis of CO_2 carbon isotopic composition in fluid inclusions. Chinese Journal
704 of Analytical Chemistry, 49(1), 137–143 (in Chinese).
705 Jomeh, A.E., Omran, N.R.N., Mansuri, E., Vignola, P., and Hashemzadeh, T. (2020) Electron microprobe
706 study of turquoise-group solid solutions in the Neyshabour and Meydook mines, northeast and
707 southern Iran. Canadian Mineralogist, 58, 71–83.
708 Kesler, S.E., Vennemann, T.W., Frederickson, C., Breithaupt, A., Vazquez, R., and Furman, F.C. (1997)
709 Hydrogen and oxygen isotope evidence for origin of MVT-forming brines, southern Appalachians.
710 Geochimica et Cosmochimica Acta, 61, 1513–1523.
711 Kile, D.E., and Eberl, D.D. (1999) Crystal growth mechanisms in miarolitic cavities in the Lake George
712 ring complex and vicinity, Colorado. American Mineralogist, 84(5-6), 718-724.
713 King, R.J. (2002). Turquoise. Geology Today, 18(3), 110-114.
714 Lawler, J.P., and Crawford, M.L. (1983) Stretching of fluid inclusions resulting from a low-temperature
715 microthermometric technique. Economic Geology, 78, 527–52.
716 Legros, H., Lecumberri-Sanchez, P., Elongo, V., Laurent, O., Falck, H., Adlakha, E., and
717 Chelle-Michou, C. (2020) Fluid evolution of the Cantung tungsten skarn, Northwest Territories,

718 Canada: Differentiation and fluid-rock interaction. Ore Geology Reviews, 127, 103866.
719 Leventhal, J.S., and Giordano, T.H. (1997) The nature and roles of organic matter associated with ores
720 and ore-forming systems: an introduction. In T. H. Giordano, R.M. Kettler and S.A. Wood, Eds.,
721 Ore Genesis and Exploration: The Roles of Organic Matter. Reviews in Economic Geology, 9, p.
722 1-26.
723 Li, N., Deng, J., Yang, L.Q., Goldfarb, R.J., Zhang, C., Marsh, E., Lei, S.B., Koenig, A., and Lowers, H.,
724 (2014) Paragenesis and geochemistry of ore minerals in the epizonal gold deposits of the Yangshan
725 gold belt, West Qinling, China. Mineralium Deposita, 49, 427-449.
726 Li, N., Chen, Y.J., Santosh, M., and Pirajno, F. (2015) Compositional polarity of Triassic granitoids in
727 the Qinling Orogen, China: implication for termination of the northernmost paleo-Tethys.
728 Gondwana Research, 27, 244–257.
729 Li, Q., and Zhao, J.H. (2016) Petrogenesis of the Wudang mafic dikes: Implications of changing tectonic
730 settings in South China during the Neoproterozoic. Precambrian Research, 272, 101-114.
731 Li, Q., Li, J, and Zhu, B.L. (2022) Experimental investigation of the influence of sequential water-rock
732 reactions on the mineral alterations and porosity evolution of shale. Construction and Building
733 Materials, 317, 125859.
734 Lin, C.Q., Hu, M., and He, H.T. (2006) Ore-control conditions and prospecting direction of silver-gold
735 polymetallic deposit in Wudang Area, Hubei Province. Contributions to Geology and Mineral
736 Resources Research, 21(02), 104-108 (in Chinese).
737 Ling, W.L., Chen, J.P., Wang, X.H., and Zhou, H.W. (2002) Geochemical features of the
738 Neoproterozoic igneous rocks from the Wudang region and their implications for the reconstruction
739 of the Jinning tectonic evolution along the south Qinling orogenic belt. Acta Petrologica Sinica, 18,
740 25–36 (in Chinese with English abstract).
741 Ling, W.L., Ren, B.F., Duan, R.C., Liu, X.M., Mao, X.W., Peng, L.H., Liu, Z.X., Chen, J.P., and Yang,
742 H.M. (2007) Timing of the Wudangshan, Yaolinghe volcanic sequences and mafic sills in South
743 Qinling: U–Pb zircon geochronology and tectonic implication. Chinese Science Bulletin, 52, 1445–
744 1456 (in Chinese).
745 Liu, L., Yang, M., and Li, Y. (2020) Unique raindrop pattern of turquoise from Hubei, China. Gems &
746 Gemology, 56(3), 380-400.

747 Liu, S.C., Ning, S.Y., and Zheng, D.S. (2021) Petrogenesis and sedimentary environment of black rock
748 series of the Lowe Cambrian Shuigoukou Formation in South Qinling. Acta Geologica Sinica,
749 95(2), 549-564 (in Chinese).
750 Lueders, V., Plessen, B., and di Primio, R. (2012) Stable carbon isotopic ratios of CH_4-CO_2-bearing
751 fluid inclusions in fracture-fill mineralization from the Lower Saxony Basin (Germany) – A tool for
752 tracing gas sources and maturity. Marine and Petroleum Geology, 30, 174-193.
753 Ma, Y., Jiang, S.Y., Frimmel, H.E., Zhu, L.Y., Xiong, S.F., Chen, R.S., and Li, X.X. (2021) Genesis of
754 the Hebaoshan gold deposit in Fujian Province of Southeast China: constraints from a combined
755 fluid inclusion, H-O-C-S-Pb-He-Ar isotope and geochronological study. Mineralium Deposita, 57(1),
756 13–34.
757 Menzies, C.D., Teagle, D.A.H., Craw, D., Cox, S.C., Boyce, A.J., Barrie, C.D., and Roberts, S. (2014)
758 Incursion of meteoric waters into the ductile regime in an active orogen. Earth and Planetary Science
759 Letters, 399,1-13.
760 Mernagh, T.P., and Wilde, A.R. (1989) The use of the laser Raman microprobe for the determination of
761 salinity in fluid inclusions. Geochimica et Cosmochimica Acta, 53, 765–771.
762 Nie, H., Wan, X., Zhang, H., He, J.F., Hou, Z.H., Siebel, W., and Chen, F.K. (2016) Ordovician and
763 Triassic mafic dykes in the Wudang terrane: Evidence for opening and closure of the South Qinling
764 ocean basin, central China. Lithos, 266-267, 1-15.
765 Niu, P.P., Jiang, S.Y., Li, W.T., Cui, P.L., Chen, Y.C., and Munoz, M. (2022) Hydrothermal evolution
766 and origin of the Suixian molybdenum deposit in the Tongbai orogenic belt, China: Constraints from
767 geology, fluid inclusions and multiple isotopes (H-O-C-S-Pb). Ore Geology Reviews, 148, 105036.
768 Ohmoto, H. (1972) Systematics of sulfur and carbon isotopes in hydrothermal ore deposits. Economic
769 Geology, 67, 551–578.
770 Phillips, G.N., and Powell, R. (2010) Formation of gold deposits: a metamorphic devolatilization model.
771 Journal of Metamorphic Geology, 28, 689-718.
772 Pirard, C., Hatert, F., and Fransolet, A.M. (2007) Alteration sequences of aluminium phosphates from
773 Montebras pegmatite, Massif Central, France. In T. Martins and R. Vieira, Eds., In Proceedings of
774 the Granitic Pegmatites: The State of the Art-International Symposium, Porto, Portugal, p. 74-75.
775 Qin, Y., and Zhou, Z.J. (2009) Organic geochemistry characteristics of Yangshan super-large gold

776 deposit, Gansu province. Acta Petrologica Sinica, 25, 2801-2810 (in Chines with English abstract).
777 Qin, Y., Xu, Y.Y., Li, H.M., Li, S.X., and Xi, Q.F. (2015) Turquoise Mine and Artefact Correlation for
778 Some Bronze Age Archaeological Sites in Hubei Province, China. Archaeometry, 57(5), 788-802.
779 Ramboz, C., Pichavant, M., and Weisbrod, A. (1982) Fluid immiscibility in natural processes: Use and
780 misuse of fluid inclusion data. II. Interpretation of fluid inclusion data in terms of immiscibility.
781 Chemical Geology, 37, 29–48.
782 Ribeiro, R., Capela, D., Ferreira, M., Martins, R., Jorge, P., Guimarães, D., and Lima, A. (2021) X-ray
783 fluorescence and laser-induced breakdown spectroscopy analysis of Li-rich minerals in veins from
784 Argemela Tin Mine, central Portugal. Minerals, 11(11), 1169.
785 Roedder, E. (1984) Fluid inclusions. Reviews in Mineralogy, 12, 1-644.
786 Rossi, M., Rizzi, R., Vergara, A., Capitelli, F., Altomare, A., Bellatreccia, F., Saviano, M., and Ghiara,
787 R.M. (2017) Compositional variation of turquoise-group minerals from the historical collection of
788 the Real Museo Mineralogico of the University of Naples. Mineralogical Magazine, 81(6),
789 1405-1429.
790 Schoell, M. (1980) The hydrogen and carbon isotopic composition of methane from natural gases of
791 various origins. Geochimica et Cosmichimica Acta, 44, 649-661.
792 Shepherd, T.J., Bottrell, S.H., and Miller, M.F. (1991) Fluid inclusion volatiles as an exploration guide
793 to black shale-hosted gold deposits, Dolgellau gold belt, North Wales UK. Journal of Geochemical
794 Exploration, 42, 5–24.
795 Sheppard, S.M.F. (1986) Characterization and isotope variations in natural waters. Reviews in
796 Mineralogy and Geochemistry, 16(1), 165-183.
797 Shi, Z.R., and Cai, K.Q. (2011) A study of the origin of turquoise deposit in Zhushan County, Hubei
798 Province. Acta Petrologica et Mineralogica, 30, 187-194 (in Chinese with English abstract).
799 Skora, S., Baumgartner, L.P., Mahlen, N.J., Johnson, C.M., Pilet, S., and Hellebrand, E. (2006)
800 Diffusion-limited REE uptake by eclogite garnets and its consequences for Lu-Hf and Sm-Nd
801 geochronology. Contributions to Mineralogy and Petrology, 152, 703-720.
802 Stepanov, A.S. (2021) A review of the geochemical changes occurring during metamorphic
803 devolatilization of metasedimentary rocks. Chemical Geology, 568, 120080.
804 Szakáll, S., Kristály, F., and Zajzon, N. (2012) Minerals of turquoise group from Sândominic, Gurghiu

Mts., Romania and from Parádfürdő, Mátra Mts., Hungary. In Acta Mineralogica-Petrographica, Abstract series, 7, 133.

Taghipour, B., and Mackizadeh, M.A. (2014) The origin of the tourmaline-turquoise association hosted in hydrothermally altered rocks of the Kuh-Zar Cu-Au-turquoise deposit, Damghan, Iran. Neues Jahrbuch für Geologie und Paläontologie – Abhandlungen, 272, 61–77.

Tarantola, A., Mullis, J., Vennemann, T., Dubessy, J., and de Capitani, C. (2007) Oxidation of methane at the CH_4/H_2O-(CO_2) transition zone in the external part of the Central Alps, Switzerland: Evidence from stable isotope investigations. Chemical Geology, 237, 329–357.

Taylor, H.P. (1974) The application of oxygen and hydrogen isotope studies to problems of hydrothermal alteration and ore deposition. Economic Geology, 69, 843–883.

Taylor, B.E. (1986) Magmatic volatiles: isotopic variation of C, H, and S. Reviews in Mineralogy and Geochemistry, 16, 185–225.

Tu, H.K. (1996) Geological characteristics of turquoise ore in the areas adjacent to Shanxi and Hubei Province. Geology of Shanxi, 14(2), 59–64 (in Chinese).

Tu, H.K. (1997) Metallogenic characteristics of turquoise in East Qinling Mountains. Non-Metallic Geology, 92(3), 24–25 (in Chinese).

Ubide, T., McKenna, C.A., Chew, D.M., and Kamber, B.S. (2015) High-resolution LA-ICP-MS trace element mapping of igneous minerals: in search of magma histories. Chemical Geology, 409, 157-168.

Veizer, J., Holser, W.T., and Wilgus, C.K. (1980) Correlation of $^{13}C/^{12}C$ and $^{34}S/^{32}S$ secular variations. Geochimica et Cosmochimica Acta, 44, 579–587.

Walrafen, G.E. (1964) Raman spectral studies of water structure. Journal of Chemical Physics 40, 3249–3256.

Walrafen, G.E. (1967) Raman spectral studies of effects of temperature on water structure. Journal of Chemical Physics, 47, 114–126.

Wang, D.S., Wang, Z.Q., Wang, G., Wu, Y.D., and Yang, H. (2019) Metamorphism of Rocks in Shiyan-Wudang Area of South Qinling Tectonic Belt, China. Journal of Earth Sciences and Environment, 41, 379-395 (in Chinese with English abstract).

Wang, L.S. (2009) Study on the metallogenic regularity and geological-geochemistry for black rock

834 series and related typical deposits in Qinling Mountains, Shanxi, 165 p. Ph.D. thesis, Northwest
835 University (in Chinese with English abstract).
836 Wang, Y.S. (2016) The study of sequence and mineralization of black shales in Shuigoukou Formation,
837 Southwestern Henan, 55 p. M.D. thesis, China University of Geosciences (Beijing) (in Chinese
838 with English abstract).
839 Xia, R., Deng, J., Qing, M., Wang, C.M., and Li, W.L. (2013) The genesis of the Dachang gold ore field
840 in Qinghai Province: Constraints on fluid inclusion geochemistry and H-O isotopes. Acta
841 Petrologica Sinica, 29, 1358-1376 (in Chinese with English abstract).
842 Xu, G.J. (1998) A fluid inclusion study of syntectonic Zn-Pb-Ag mineralization at Dugald River,
843 northwest Queensland, Australia. Economic Geology and the Bulletin of the society of economic
844 geologists, 93(8). 1165-1179.
845 Yardley, B.W.D. (1989) An Introduction to Metamorphic Petrology. Longman Scientific and Technical,
846 Harlow.
847 Yardley, B.W.D., and Graham, J.T. (2002) The origins of salinity in metamorphic fluids. Geofluids, 2(4),
848 249-256.
849 You, J., Cao, H.Y., Zhang, F.J., Cai, W.C., Li, J.C., and She, P.T. (2018) Geochemical characteristics of
850 strata of Lower Cambrian Shuigoukou Formation in Southern Qinling and their implications for
851 prospecting. Geophysical and Geochemical Exploration, 42(3), 453-460.
852 Yue, S.W., Deng, X.H., and Bagas, L. (2014) Geology, isotope geochemistry, and ore genesis of the
853 Yindonggou Ag-Au(-Pb-Zn) deposit, Hubei Province, China. Geological Journal, 49, 442-462.
854 Zhang, G.W., Zhang, Z.Q., and Dong, Y.P. (1995) Nature of main tectonolithostratigraphic units of the
855 Qinling Orogen: implications for the tectonic evolution. Acta Petrologica Sinica, 11, 101–114 (in
856 Chinese with English abstract).
857 Zhang, G.W., Zhang, B.R., Yuan, J.C., and Xiao, Q.H. (2001) Qinling Orogenic Belt and Continental
858 Dynamics. Science Press: Beijing; 1–855 (in Chinese).
859 Zhang, J., Yu, X.Z., and Li, Y.C. (2019) Minerogenic prospective prognosis of leaching type turquoise
860 on the northwestern margin of Wudang Uplift. Geophysical and Geochemical Exploration, 43(2),
861 273-280 (in Chinese).
862 Zhang, Z.Q., Zhang, G.W., Tang, S.H., and Wang, J.H. (2002) The age of metamorphic rocks of the

Wudang Group. Geology in China, 29, 117–125 (in Chinese with English abstract).

Zhao, X.K., Li, J.L., Liu, Y.L., and R.K. (2017) Resource overview and genesis of Baihe turquoise deposit in Ankang City. Geology of Shaanxi, 35, 46-51 (in Chinese).

Zhou, D.W., Zhang, C.L., Liu, L., Wang, J.L., Liu, Y.Y., and Zhang, Z.Q. (1998) Sm–Nd dating of basic dykes from Wudang block and a discussion of related questions. Acta Geoscientia Sinica, 19, 25–30 (in Chinese with English abstract).

Zhou, L.L., McKenna, C.A., Long, D.G.F., and Kamber, B.S. (2017) LA-ICP-MS elemental mapping of pyrite: An application to the Paleoproterozoic atmosphere. Precambrian Research, 297, 33-55.

Zhou, J.X., Bai, J.H., Huang, Z.L., Zhu, D., Yan, Z.F., and Lv, Z.C. (2015) Geology, isotope geochemistry and geochronology of the Jinshachang carbonate-hosted Pb-Zn deposit, southwest China. Journal of Asian Earth Sciences, 98, 272-284.

Figure captions

Fig. 1. (**a**) A tectonic map of China showing the location of the Qinling Orogen (red square); (**b**) Tectonic subdivision of the Qinling Orogen comprising the Wudang Block (red square) where occur the turquoise deposits; (**c**) Geological map of the turquoise deposits in Zhushan County, western Hubei Province of China (modified after Yue et al., 2014; Zhang et al., 2019) (*YB:* Yangtze Block, *NCB:* North China Block).

Fig. 2. Photographs representing typical field occurrence of turquoise-bearing veins from Zhushan County. (**a**) Quartz-barite-turquoise vein as fracture infillings along or cross-cutting the beddings of the black carbonaceous slate; (**b**) coexisting turquoise and quartz as elongated lenses in the ductile deformed veins; (**c, d**) massive turquoise aggregates in the black carbonaceous slates show synchronous ductile deformation with wall rocks (*Trq:* turquoise, *Qtz:* quartz, *Brt:* barite, red lines outlining the elongated lens-shaped quartz, barite and turquoise, rock hammer as scale bar is approximately 13 cm in width).

Fig. 3. Photographs of turquoise from Zhushan County. (**a**) Massive bluish green turquoise in black slate; (**b**, **c**, **d**) Vein specimens consisting of quartz, barite and turquoise in different colors, i.e. bluish-green (b) and light-green (c, d) (*Trq:* turquoise, *Qtz:* quartz, *Brt:* barite).

Fig. 4. Transmitted- (**a, d**), reflected-light (**e**) and back scattered electron (BSE) images (**b-c, f-h**), showing representative mineralogical and textural features observed in hydrothermal veins and wall rocks: (**a**) oscillatory zoned turquoise (Trq^{II}) replacing homogeneous turquoise (Trq^{I}) along the margin, all included in quartz (Qtz^{I}) and cut by irregular barite vein (Brt^{II}); (**b**) quartz (Qtz^{I}) intergrowth with homogeneous turquoise (Trq^{I}) and euhedral barite (Brt^{I}); (**c**) oscillatory zoned turquoise (Trq^{II}) filled by anhedral barite (Brt^{II}) in quartz vein (Qtz^{II}); (**d**) preferred orientation of fine-grained quartz defining the foliations of the carbonaceous slate, showing typical rotational porphyroclast system; (**e**) intense

foliation defined by alignment of elongated coarse-grained magnetite and fine-grained muscovite in the deformed carbonaceous slate; (**f-h**) medium to coarse-grained pyrite, magnetite, apatite, monazite, rutile and xenotime surrounded by quartz and muscovite (*Trq:* turquoise, *Qtz:* quartz, *Brt:* barite; *Ms:* muscovite, *Ap:* apatite, *Mag:* magnetite, *Py:* pyrite, *Rt:* rutile, *Mnz:* monazite, *Xtm:* xenotime).

Fig. 5. BSE image and characteristic chemical compositions collected from homogeneous turquoise (Trq^{I}) and oscillatory zoned turquoise (Trq^{II}) in from the rim to core: (**a**) BSE image; (**b-f**) major element compositions of turquoise-group minerals, where blue circles represent the compositions of Trq^{I}, and dark green to light green circles refer to the various compositions of Trq^{II} from the core to rim. EPMA data and corresponding unit formula (apfu) are from Table 1 (*Trq:* turquoise, *Qtz:* quartz).

Fig. 6. (**a**) Cu (apfu) *versus* A site (apfu); (**b**) Water contents (wt.%) *versus* A site (apfu) of all EPMA data of turquoise-group minerals from Table 1 (modified after Foord and Taggart, 1998).

Fig. 7. BSE image coupled with LA-ICP-MS elemental maps of a turquoise grain. (*Trq:* turquoise, *Qtz:* quartz).

Fig. 8. Photomicrographs of different types of fluid inclusions in quartz and barite: (**a**) Type I aqueous-carbonic fluid inclusion; (**b, c**) primary fluid inclusion trail containing Type I and II fluid inclusions with various vapor/liquid ratios along the growth faces of quartz; (**d**) pseudosecondary fluid inclusion assemblage consisting of Type II and III fluid inclusions in barite; (**e, f**) pseudosecondary fluid inclusion assemblage consisting of Type II inclusions at +23 °C and -190 °C in quartz. (*Qtz:* quartz, *Brt:* barite, *S*: solid phase in fluid inclusion as daughter mineral or accidently trapped solid).

Fig. 9. Laser Raman spectra of representative fluid inclusions in quartz and barite: (**a**) Raman spectrum of the aqueous phase in Type I fluid inclusion showing peaks of propane (2886 cm^{-1}), ethane (2943 cm^{-1}), and H_2O (3419 cm^{-1}); (**b**) Raman spectrum of vapor phase in Type I inclusion, showing significant contents of N_2 (2327 cm^{-1}) and CH_4 (2917 cm^{-1}); (**c**) Raman spectrum for Type II pure carbonic fluid inclusions, showing typical peaks of N_2 (2327cm^{-1}) and CH_4 (2917 cm^{-1}); (**d**) Raman spectra for vapor and liquid phases of Type III aqueous-salt fluid inclusions, showing the narrower and more symmetrical water peaks.

Fig. 10. Histograms of (**a**, **e**) final ice melting temperature ($T_{m,\ ice}$), (**b**, **f**) salinity, (**c**, **g**) total homogenization temperature (T_h), (**d**, **h**) total homogenization temperature after pressure correction (Pressure-corrected T_h) of Type I_b, Type II and Type III fluid inclusions in quartz and barite. Average values with standard deviations are sourced from Table 2. (*Qtz:* quartz, *Brt:* barite).

Fig. 11. Isochore plots calculated from Type I_b H_2O-CH_4-NaCl and Type III H_2O-NaCl fluid inclusions identified in the quartz-barite-turquoise vein from Zhushan County, western Hubei Province of China.

Fig. 12. Paragenetic diagram and simplified sketch drawings showing the turquoise-related minerals and their enclosed fluid inclusions: (**a**) diagram showing relative timing of minerals associated with turquoise; (**b**) microthermometric charts showing ranges of pressure-corrected homogenization temperatures (T_h) and salinity, where fluid inclusions of different types are labelled with various colors, the same as Fig. 10;

(**c**, **d**) drawings showing the distributions of fluid inclusions of various types enclosed in the quartz and barite at room temperature. (*Trq:* turquoise, *Qtz:* quartz, *Brt:* barite, *Fls:* fluid inclusions).

Fig. 13. (**a**) Hydrogen *versus* calculated oxygen isotopic compositions diagram indicating ore fluid compositions from the turquoise deposit in Zhushan County, western Hubei Province of China. Also shown are fields for metamorphic fluids (Taylor, 1974), magmatic water (Hedenquist and Lowenstern,1994), and organic water (Sheppard, 1986); (**b**) comparison of carbon isotopic compositions of CO_2 in the quartz fluid inclusions with data for various carbon sources (data after Veizer et al., 1980; Taylor, 1986; Ohmoto, 1972; Hou, 2008).

Table captions

Table 1. EPMA data (wt%) and calculated unit formula (apfu), based on 11 cations, for turquoise-group minerals from Zhushan County.

Table 2. Summary of microthermometic data of fluid inclusions from the quartz-barite-turquoise vein in Zhushan County.

Table 3. Raman spectra and band assignment of the individual fluid inclusion.

Table 4. Hydrogen, oxygen and carbon isotope analyses of quartz and fluid inclusions from the quartz-barite-turquoise vein in Zhushan County.

CRediT authorship contribution statement

WTL: Methodology, Formal analysis, Investigation, Writing - Original Draft; SYJ: Conceptualization, Resources, Supervision, Funding acquisition, Writing - Review & Editing; HZ and PLC: Methodology, Resources.

Declaration of competing interest

The authors declare that they have no known competing financial interests or personal relationships that could have appeared to influence the work reported in this paper.

Data and materials availability

All the data used in this paper are listed as Tables 1-4 within this paper, and are also available from the corresponding author on reasonable request.

Table 1

EPMA data (wt%) and unit formula (apfu), based on 11 cations, for turquoise-group minerals from Zhushan country.

	1	2	3	4	5	6	7	8	9	10	11	12	13
	Trq^{I} in quartz-barite vein				Trq^{II} in quartz-barite vein							Trq^{I} in wall rock	
Al_2O_3	37.52	37.01	37.98	37.85	38.14	37.55	37.58	38.49	38.98	39.76	40.34	37.66	38.12
P_2O_5	36.48	37.84	36.05	36.42	37.19	36.53	36.29	37.29	36.31	37.84	37.20	34.81	35.19
SiO_2	0.00	0.00	0.00	0.01	0.00	0.04	0.02	0.03	0.03	0.00	0.04	0.00	0.00
CuO	8.35	8.04	8.14	7.69	7.83	7.95	8.13	6.35	5.79	3.62	3.08	7.98	8.03
FeO^{T}	0.74	0.64	0.62	0.57	0.53	0.55	0.60	0.52	0.55	0.33	0.23	0.70	0.56
SO_3	0.14	0.14	0.11	0.18	0.04	0.16	0.18	0.23	0.20	0.00	0.11	0.27	0.29
ZnO	0.07	0.10	0.09	0.07	0.16	0.14	0.06	0.20	0.34	0.21	0.19	0.14	0.12
UO_2	0.02	0.04	0.10	0.04	0.00	0.00	0.00	0.00	0.00	0.04	0.06	0.01	0.02
Cr_2O_3	0.19	0.11	0.14	0.14	0.13	0.09	0.15	0.06	0.05	0.00	0.02	0.10	0.09
K_2O	0.04	0.06	0.04	0.05	0.05	0.08	0.01	0.10	0.06	0.05	0.03	0.07	0.07
V_2O_3	0.05	0.05	0.08	0.06	0.06	0.03	0.08	0.02	0.04	0.09	0.05	0.08	0.08
CaO	0.00	0.05	0.01	0.02	0.01	0.02	0.03	0.07	0.10	0.03	0.00	0.03	0.04
BaO	0.17	0.23	0.26	0.23	0.19	0.13	0.24	0.25	0.35	0.15	0.13	0.10	0.10
TiO_2	0.06	0.06	0.00	0.00	0.01	0.02	0.00	0.00	0.00	0.00	0.03	0.73	0.50
H_2O^{a}	16.10	15.61	16.39	16.68	15.64	16.68	16.65	16.38	17.17	17.84	18.50	17.32	16.82
$Total^{b}$	83.83	84.37	83.62	83.33	84.34	83.29	83.37	83.61	82.80	82.12	81.51	82.68	83.21
Total	100.00	100.00	100.00	100.00	100.00	100.00	100.00	100.00	100.00	100.00	100.00	100.00	100.00
Al	5.89	5.79	5.96	5.96	5.93	5.92	5.92	6.02	6.13	6.26	6.37	6.04	6.05
P	4.11	4.25	4.06	4.12	4.16	4.14	4.11	4.19	4.10	4.28	4.22	4.01	4.01
Cu	0.84	0.81	0.82	0.78	0.78	0.80	0.82	0.64	0.58	0.37	0.31	0.82	0.82
Fe	0.08	0.07	0.07	0.06	0.06	0.06	0.07	0.06	0.06	0.04	0.03	0.08	0.06
S	0.01	0.01	0.01	0.02	0.00	0.01	0.02	0.02	0.02	0.00	0.01	0.01	0.01
Zn	0.01	0.01	0.01	0.01	0.02	-	0.01	0.02	0.03	0.02	0.02	0.01	0.01
Cr	0.00	0.00	0.01	0.00	0.00	0.00	0.00	0.00	0.00	0.00	0.01	0.01	0.01
K	0.03	0.02	0.02	0.02	0.02	0.02	0.03	0.01	0.01	0.00	0.00	0.01	0.01
V	0.00	0.01	0.00	0.00	0.00	0.01	0.00	0.01	0.01	0.00	0.00	0.01	0.01
Ca	0.01	0.01	0.01	0.01	0.01	0.00	0.01	0.00	0.01	0.01	0.01	0.00	0.01
Ba	0.00	0.00	0.00	0.00	0.00	0.00	0.00	0.00	0.00	0.00	0.00	0.01	0.01
Ti	0.02	0.02	0.03	0.02	0.02	0.01	0.02	0.02	0.03	0.01	0.01	0.07	0.05
OH	7.24	6.44	7.57	7.25	7.11	7.08	7.24	6.90	7.43	6.84	7.16	7.91	7.93
A site	0.97	0.92	0.93	0.88	0.88	0.89	0.93	0.73	0.70	0.44	0.37	0.93	0.91
B site	5.89	5.80	5.97	5.96	5.94	5.93	5.92	6.03	6.14	6.27	6.38	6.05	6.06
T site	4.12	4.26	4.07	4.13	4.16	4.16	4.13	4.22	4.13	4.28	4.24	4.02	4.02

Notes: a: Calculated by difference; b: sum of particular components without water contents.

Table 2.

Summary of microthermometric data of fluid inclusions from the quartz-barite-turquoise vein in Zhushan country.

Host minerals[1]	Inclusion type	T_m(°C)	$T_{m,ice}$(°C)	T_h(°C)	Pressure-corrected T_h(°C)	Salinity (wt. % NaCl eq.)[2]
Quartz (Qtz^I)	Type I_a	/	-6.6--2.5	357-455	/	4.4-11.9
Quartz (Qtz^I)	Type I_b	/	-5.5--1.4 (**-3.2 ± 1.0**)	217-340 (**276 ± 37**)	347-470 (**406 ± 37**)	2.5-9.9 (**5.8 ± 1.8**)
Quartz (Qtz^I)	Type II	/	/	-145--127 (**-139 ± 6**)	/	/
Barite (Brt^I)	Type III	-24.2	-2.3--0.7 (**-1.3 ± 0.6**)	195-355 (**292 ± 43**)	325-485 (**422 ± 43**)	1.2-4.1 (**2.2 ± 1.0**)
Barite (Brt^I)	Type II	/	/	-144--126 (**-139 ± 6**)	/	/
Quartz (Qtz^{II})	Type III	-23.9--21.9	-5.2--0.9 (**-2.8 ± 0.8**)	136-315 (**239 ± 40**)	186-365 (**289 ± 40**)	1.6-9.3 (**5.0 ± 1.0**)
Quartz (Qtz^{II})	Type II	/	/	-145--126 (**-139 ± 5**)	/	/
Barite (Brt^{II})	Type III	-21.3	-2.7--1.1 (**-1.9 ± 0.6**)	222-341 (**238 ± 11**)	272-391 (**288 ± 11**)	1.8-6.6 (**4.1 ± 1.6**)

Abbreviations: T_m = First ice melting temperature; $T_{m,ice}$ = Final ice-melting temperature; T_h= analyzed temperature of final homogenization; Pressure-corrected T_h = temperature of final homogenization after the pressure correction; Type I_a = vapor-rich aqueous-carbonic fluid inclusion; Type I_b = liquid-rich aqueous-carbonic fluid inclusion; type II = carbonic fluid inclusion; Type III = aqueous-salt fluid inclusion.

[1] Mineral abbreviation is same as Fig. 4

[2] Salinities of type I and III inclusions calculated from the equation of Davis et al. (1990)

[3] In parentheses, bold number denotes the average value with standard deviations

Table 3

Raman spectra and band assignment of the individual fluid inclusion.

Wavenumber/cm^{-1}	Assignment	Raman shift of peak/cm^{-1}	Reference
2886	C_3H_8	2890	Burke, 2001
2943	C_2H_6	2954	Burke, 2001
2327	N_2	2331	Herzberg, 1950
2917	CH_4	2917/3020	Brunsgaard-Hansen et al., 2002
3419	H_2O liquid	2750-3900	Walrafen, 1964, 1967

Table 4

Hydrogen, oxygen and carbon isotope analyses of the turquoise deposit in Zhushan Country.

Min[1]	**Average pressure-corrected T_h(◦C)**	**$\delta^{18}O_{Qtz}$(‰)**	**$\delta^{18}O_{fluid}$(‰)**[2]	**δD (‰)**	**$\delta^{13}C_{CO2}$(‰)**	**$\delta^{13}C_{CH4}$(‰)**
Qtz^{I}	422	22.4	18.8	-111	-22.5	-30.3
Qtz^{I}	422	20.9	17.3	-93	-22.9	-40.8
Qtz^{II}	282	22.6	15.0	-104	-27.6	-31.3

Abbreviations: Sample no. = sample number; Min = minerals;

[1] For mineral abbreviation see Fig. 4

[2] $\delta^{18}O$ values of fluids in equilibrium with quartz were calculated using the equation of Clayton et al. (1972)

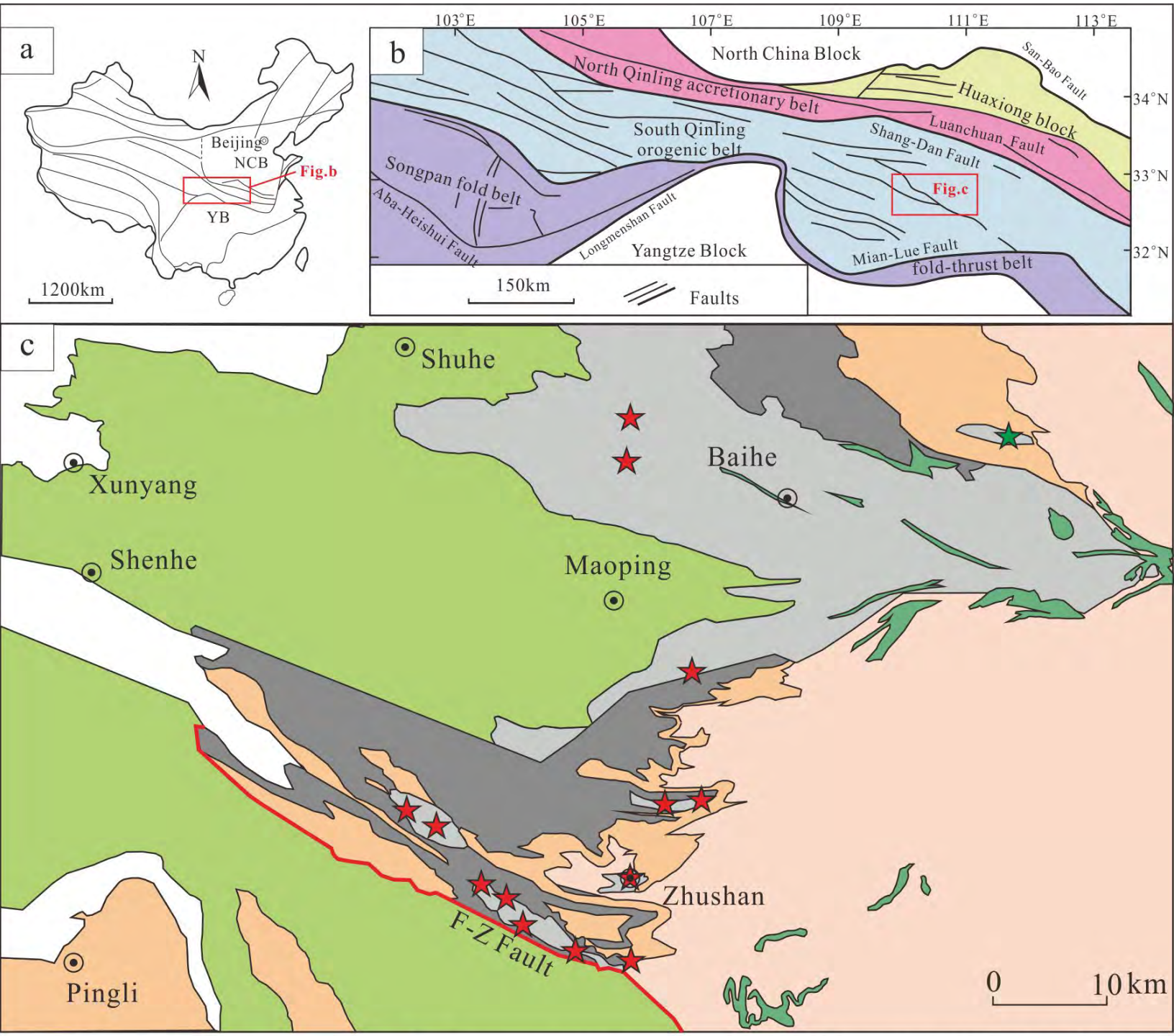
a
N
Beijing
NCB
Fig.b
YB
1200km
b
103°E
105°E
107°E
109°E
111°E
113°E
North China Block
San-Bao Fault
North Qinling accretionary belt
Huaxiong block
Luanchuan Fault
South Qinling orogenic belt
Shang-Dan Fault
Songpan fold belt
Fig.c
Aba-Heishui Fault
Longmenshan Fault
Yangtze Block
Mian-Lue Fault
fold-thrust belt
34°N
33°N
32°N
150km
Faults
c
Shuhe
Xunyang
Baihe
Shenhe
Maoping
Zhushan
F-Z Fault
Pingli
0
10km
Neoproterozoic Wudangshan Group
Neoproterozoic Yaolinghe Group
Neoproterozoic Doushantuo and Dengying Formations
Cambrian Shuigoukou Group
Silurian Meiziya Group
Mesozoic and Cenozoic units
Mafic rocks
Turquoise ore deposit
F-Z
Fangshan-Zhushan Fault

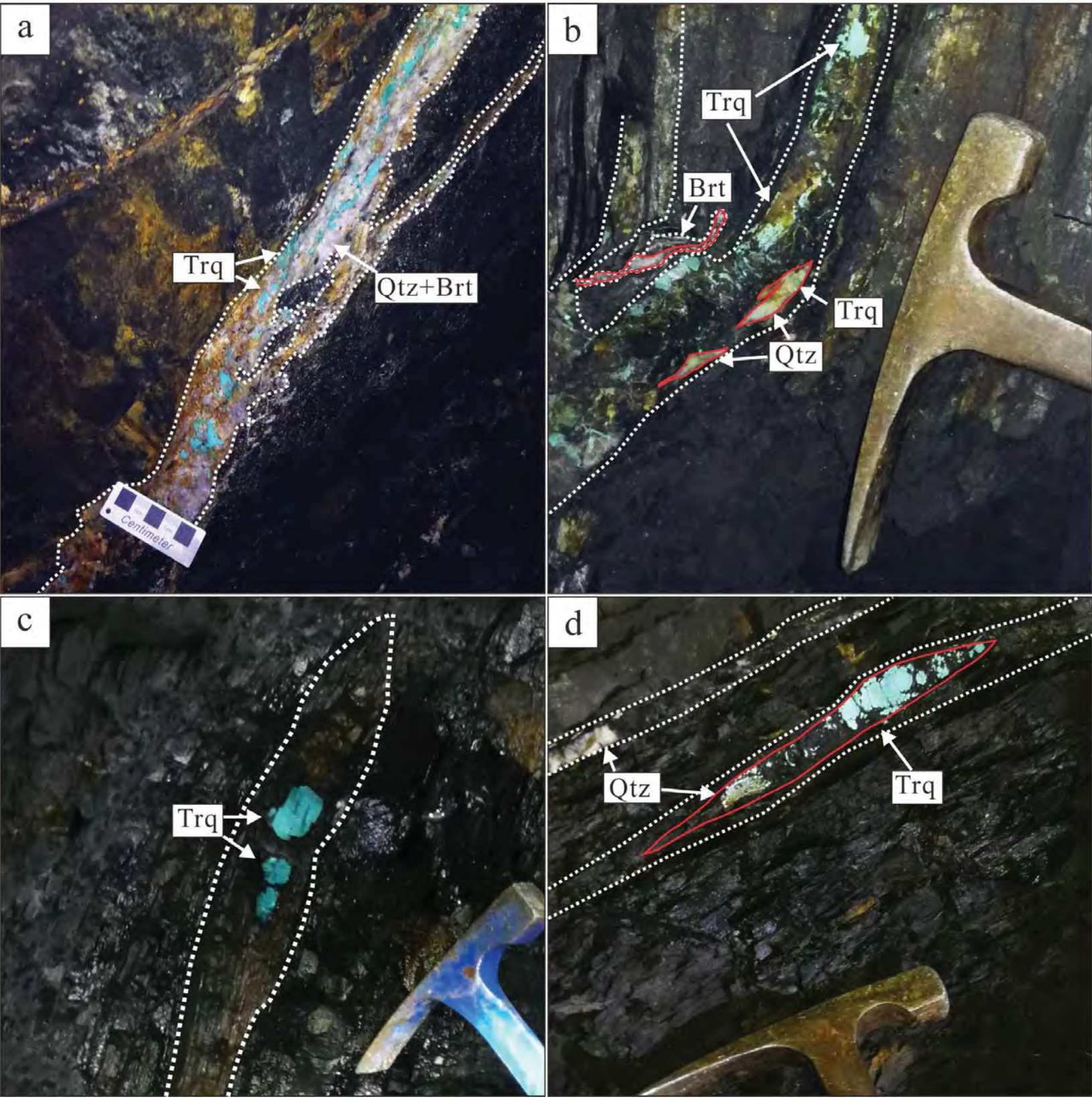
a
Trq
Qtz+Brt
Centimeter
b
Trq
Brt
Trq
Qtz
c
Trq
d
Qtz
Trq

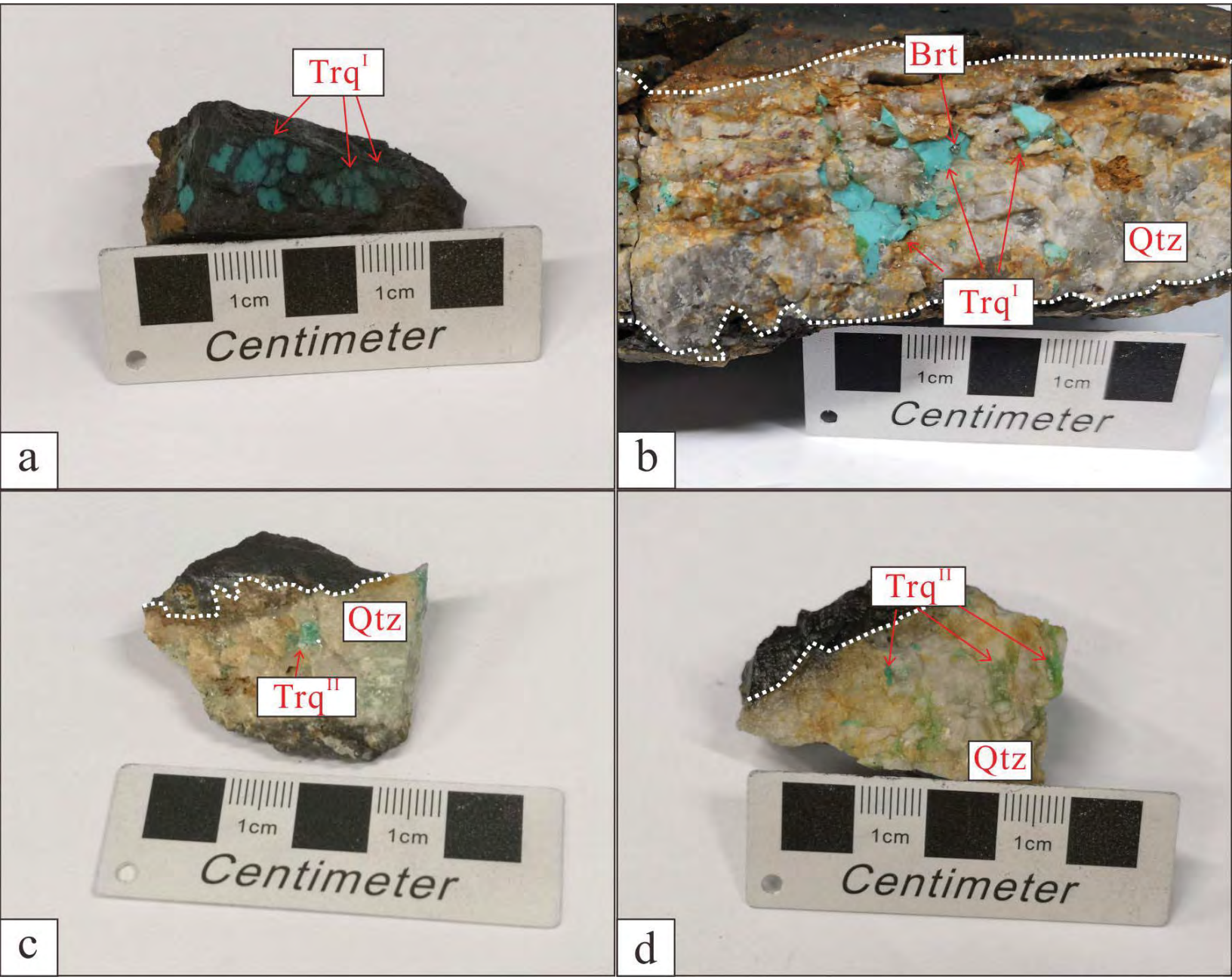
Trq^{I}
1cm
1cm
Centimeter
a
Brt
Qtz
Trq^{I}
1cm
1cm
Centimeter
b
Qtz
Trq^{II}
1cm
1cm
Centimeter
c
Trq^{II}
Qtz
1cm
1cm
Centimeter
d

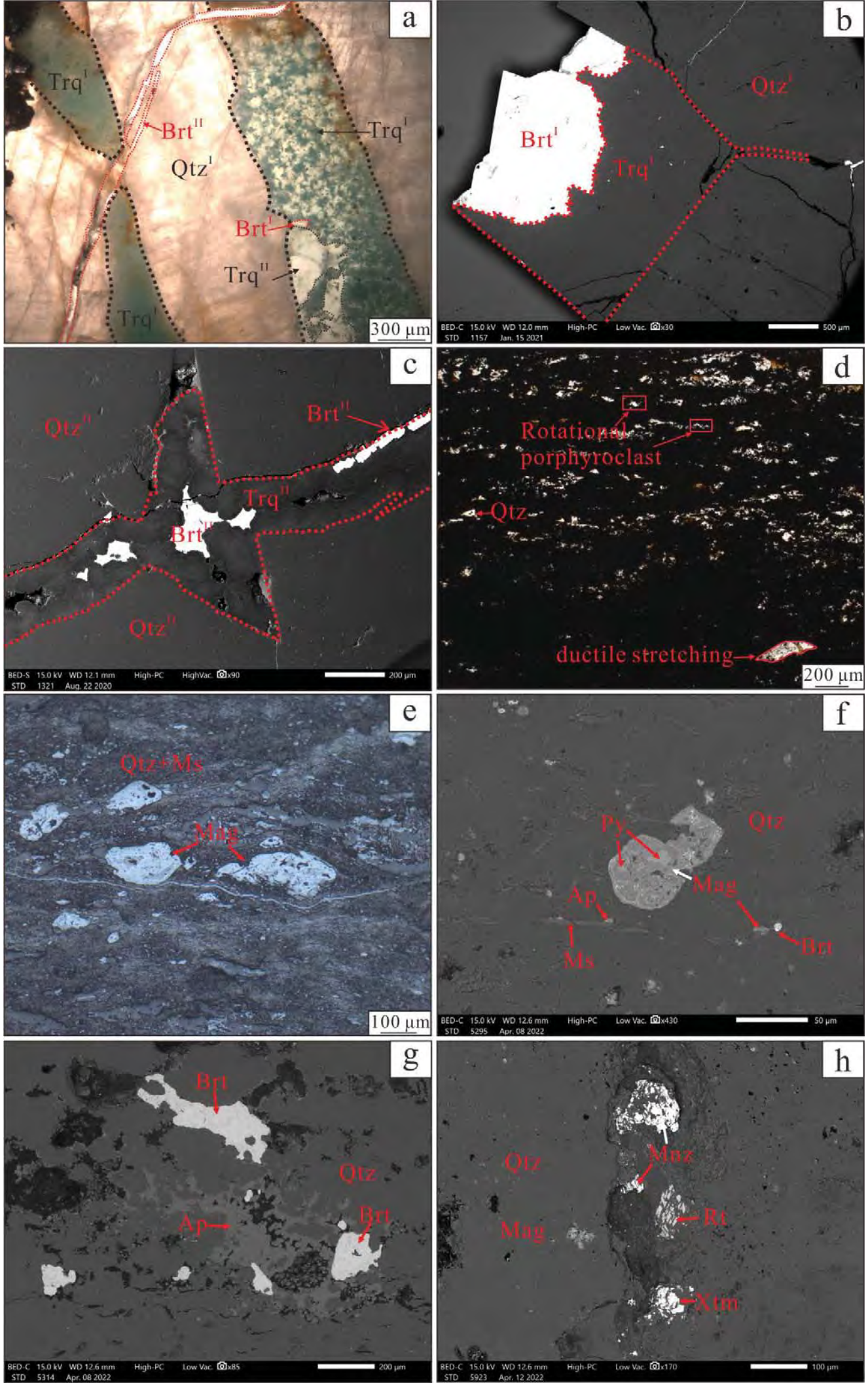
a
Trq^{I}
Brt^{II}
Trq^{I}
Qtz^{I}
Brt^{I}
Trq^{II}
Trq^{I}
300 μm
b
Qtz^{I}
Brt^{I}
Trq^{I}
BED-C 15.0 kV WD 12.0 mm High-PC Low Vac. x30 500 μm
STD 1157 Jan. 15 2021
c
Qtz^{II}
Brt^{II}
Trq^{II}
Brt^{II}
Qtz^{II}
BED-S 15.0 kV WD 12.1 mm High-PC HighVac. x90 200 μm
STD 1321 Aug. 22 2020
d
Rotational porphyroclast
Qtz
ductile stretching
200 μm
e
Qtz+Ms
Mag
100 μm
f
Py
Qtz
Ap
Mag
Ms
Brt
BED-C 15.0 kV WD 12.6 mm High-PC Low Vac. x430 50 μm
STD 5295 Apr. 08 2022
g
Brt
Qtz
Ap
Brt
BED-C 15.0 kV WD 12.6 mm High-PC Low Vac. x85 200 μm
STD 5314 Apr. 08 2022
h
Qtz
Mnz
Rt
Mag
Xtm
BED-C 15.0 kV WD 12.6 mm High-PC Low Vac. x170 100 μm
STD 5923 Apr. 12 2022

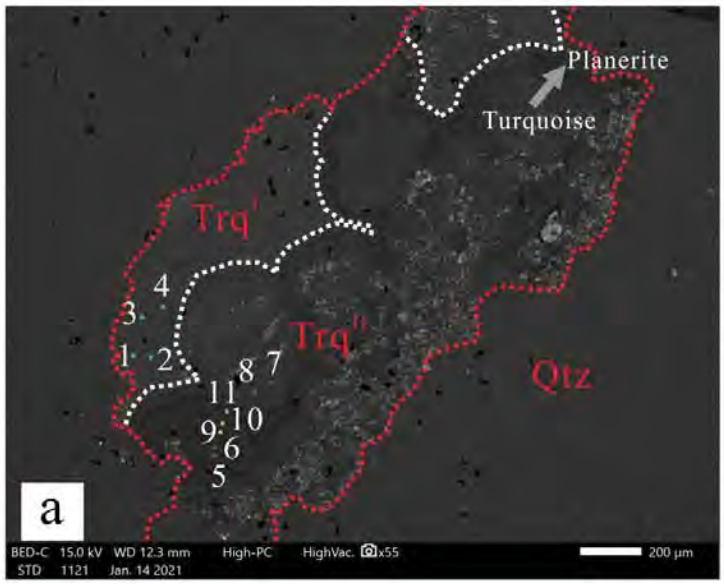
Planerite
Turquoise
Trq^{I}
Trq^{II}
Qtz
1
2
3
4
5
6
7
8
9
10
11
a
BED-C 15.0 kV WD 12.3 mm High-PC HighVac. x55 200 µm
STD 1121 Jan. 14 2021

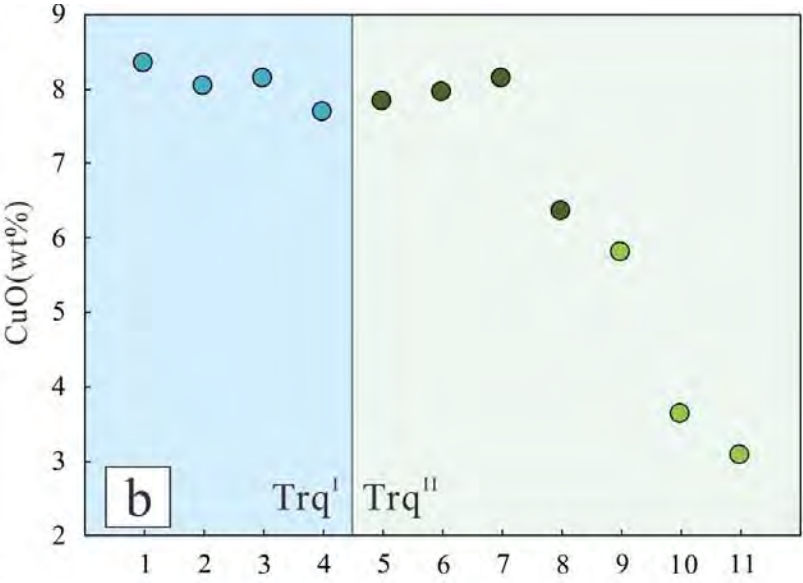
CuO(wt%)
b
Trq^{I}
Trq^{II}

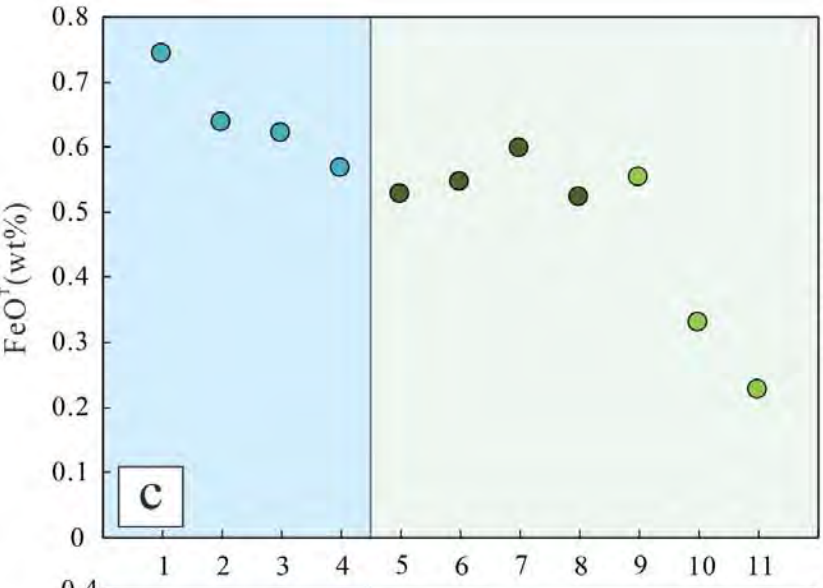
FeO^{T}(wt%)
c

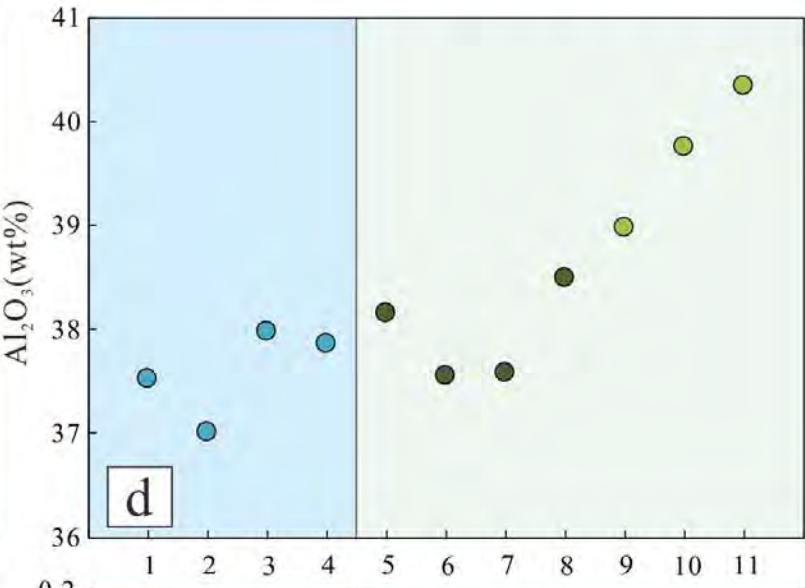
Al_2O_3(wt%)
d

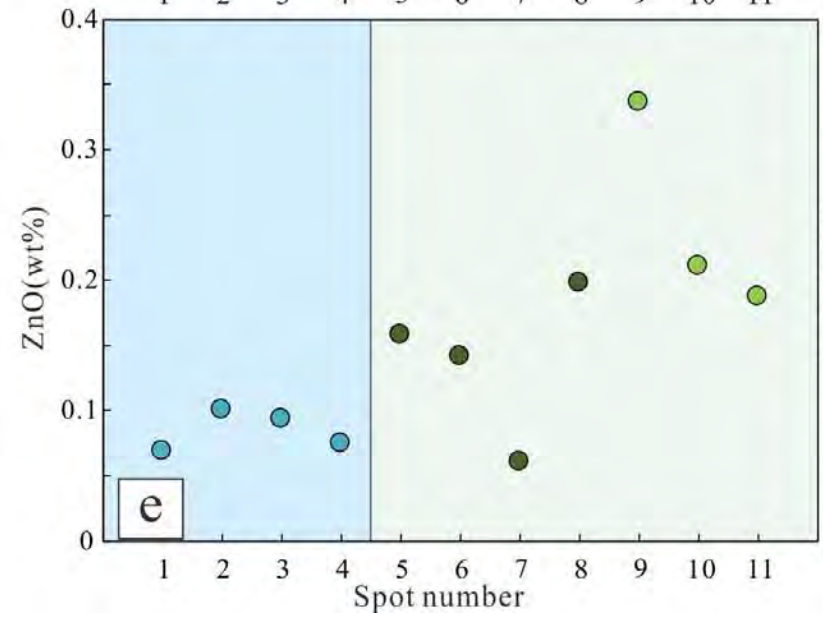
ZnO(wt%)
e
Spot number

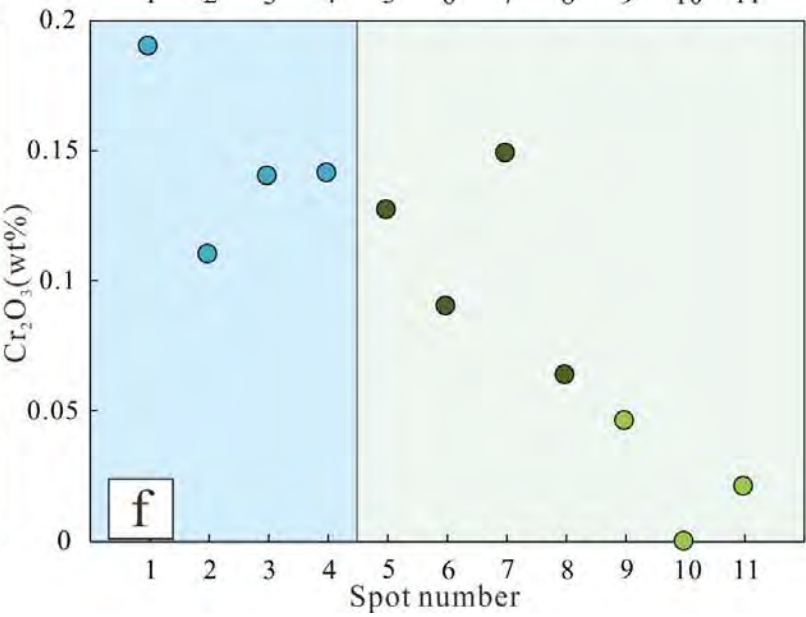
Cr_2O_3(wt%)
f
Spot number

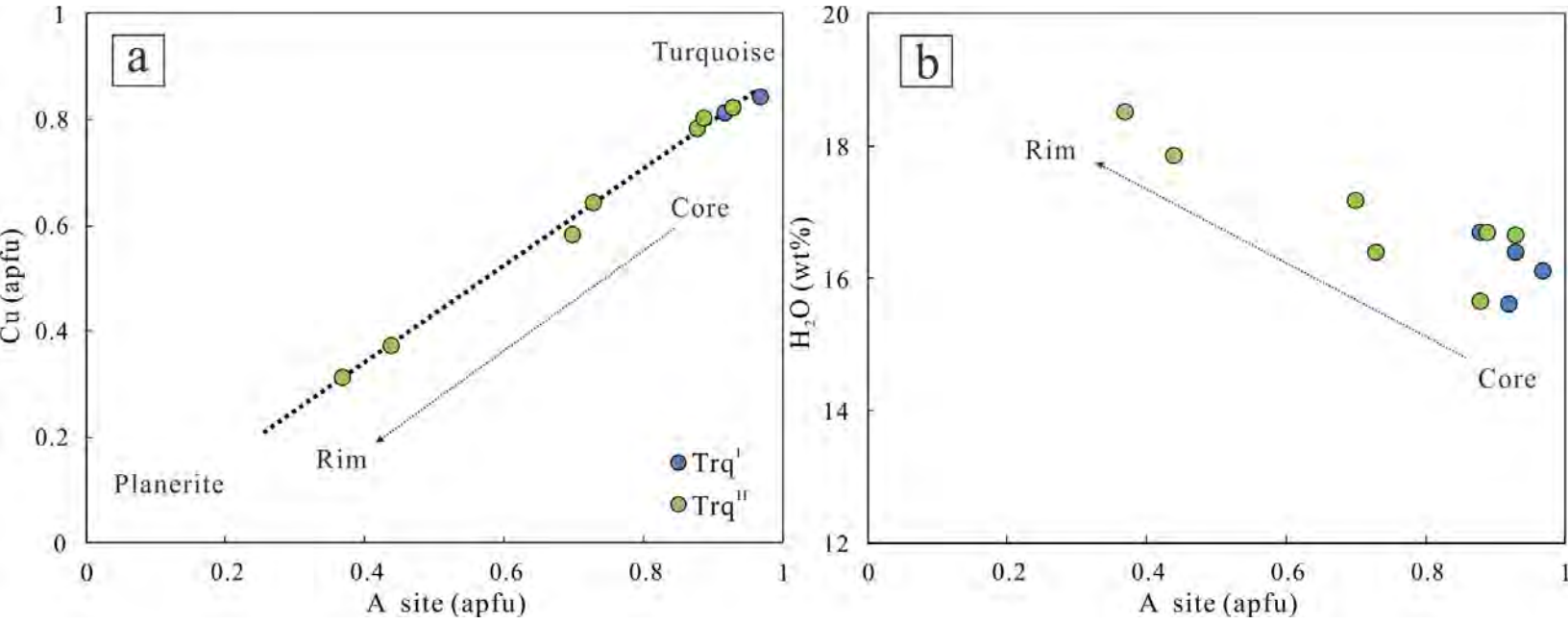
a
Turquoise
Core
Rim
Planerite
Trq^{I}
Trq^{II}
Cu (apfu)
A site (apfu)
b
Rim
Core
H_2O (wt%)
A site (apfu)

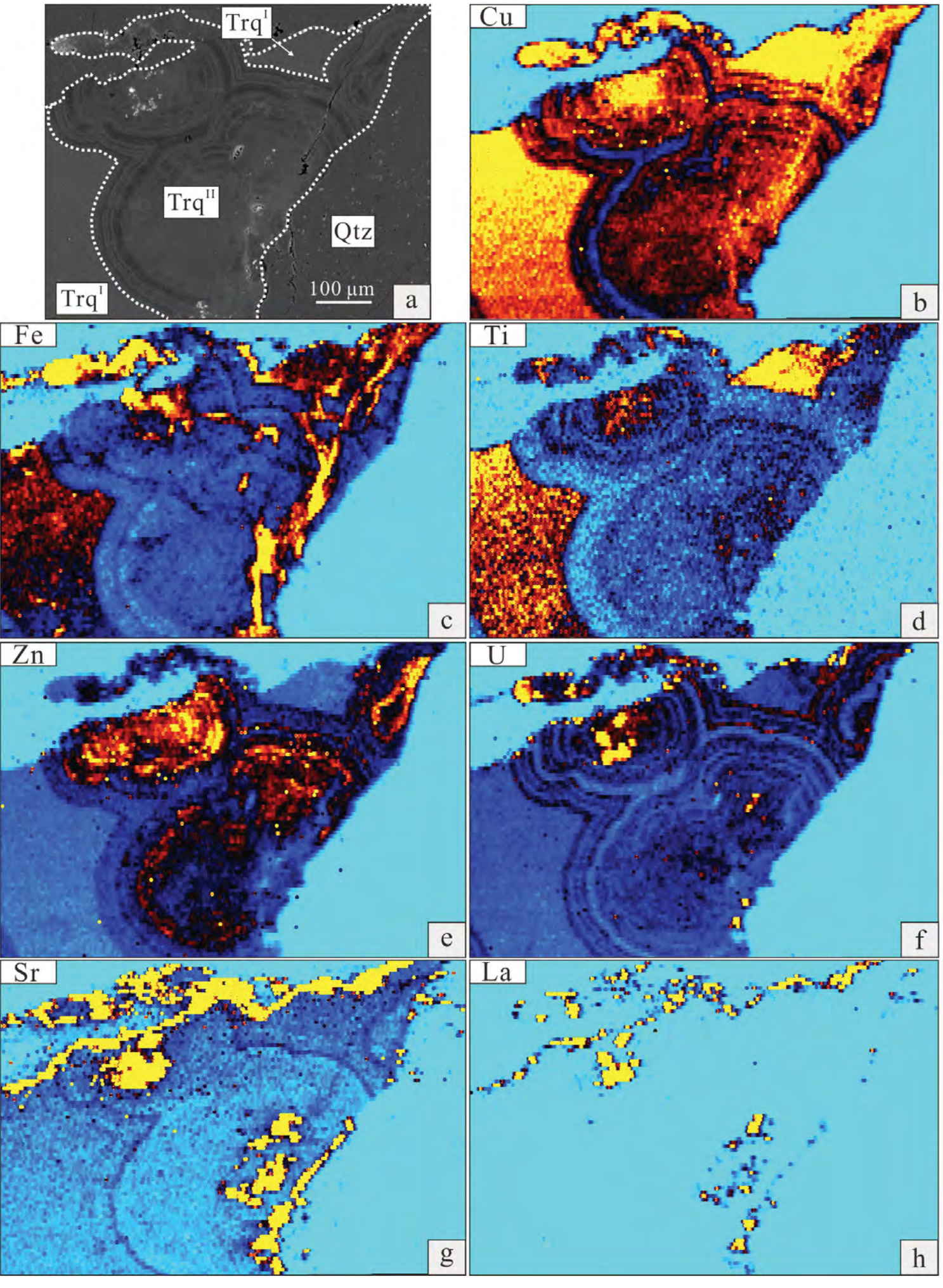
Trq^{I}
Trq^{II}
Qtz
Trq^{I}
100 µm
a
Cu
b
Fe
c
Ti
d
Zn
e
U
f
Sr
g
La
h
High
Low

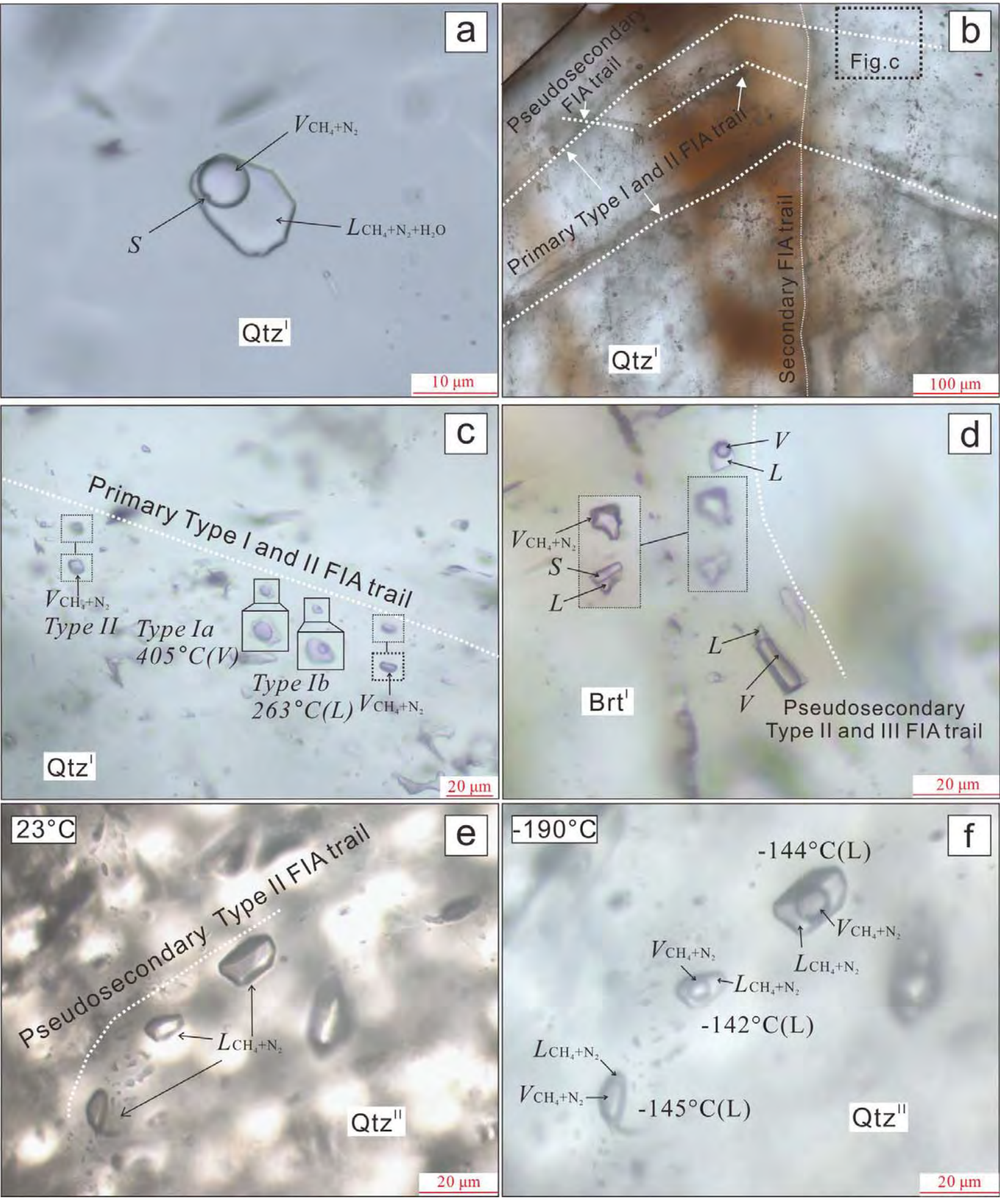
a
$V_{CH_4+N_2}$
$L_{CH_4+N_2+H_2O}$
S
Qtz^{I}
10 μm
b
Fig.c
Pseudosecondary FIA trail
Primary Type I and II FIA trail
Secondary FIA trail
Qtz^{I}
100 μm
c
Primary Type I and II FIA trail
$V_{CH_4+N_2}$
Type II
Type Ia
405°C(V)
Type Ib
263°C(L)
$V_{CH_4+N_2}$
Qtz^{I}
20 μm
d
V
L
$V_{CH_4+N_2}$
S
L
L
V
Brt^{I}
Pseudosecondary
Type II and III FIA trail
20 μm
23°C
e
Pseudosecondary Type II FIA trail
$L_{CH_4+N_2}$
Qtz^{II}
20 μm
-190°C
f
-144°C(L)
$V_{CH_4+N_2}$
$V_{CH_4+N_2}$
$L_{CH_4+N_2}$
$L_{CH_4+N_2}$
-142°C(L)
$L_{CH_4+N_2}$
$V_{CH_4+N_2}$
-145°C(L)
Qtz^{II}
20 μm

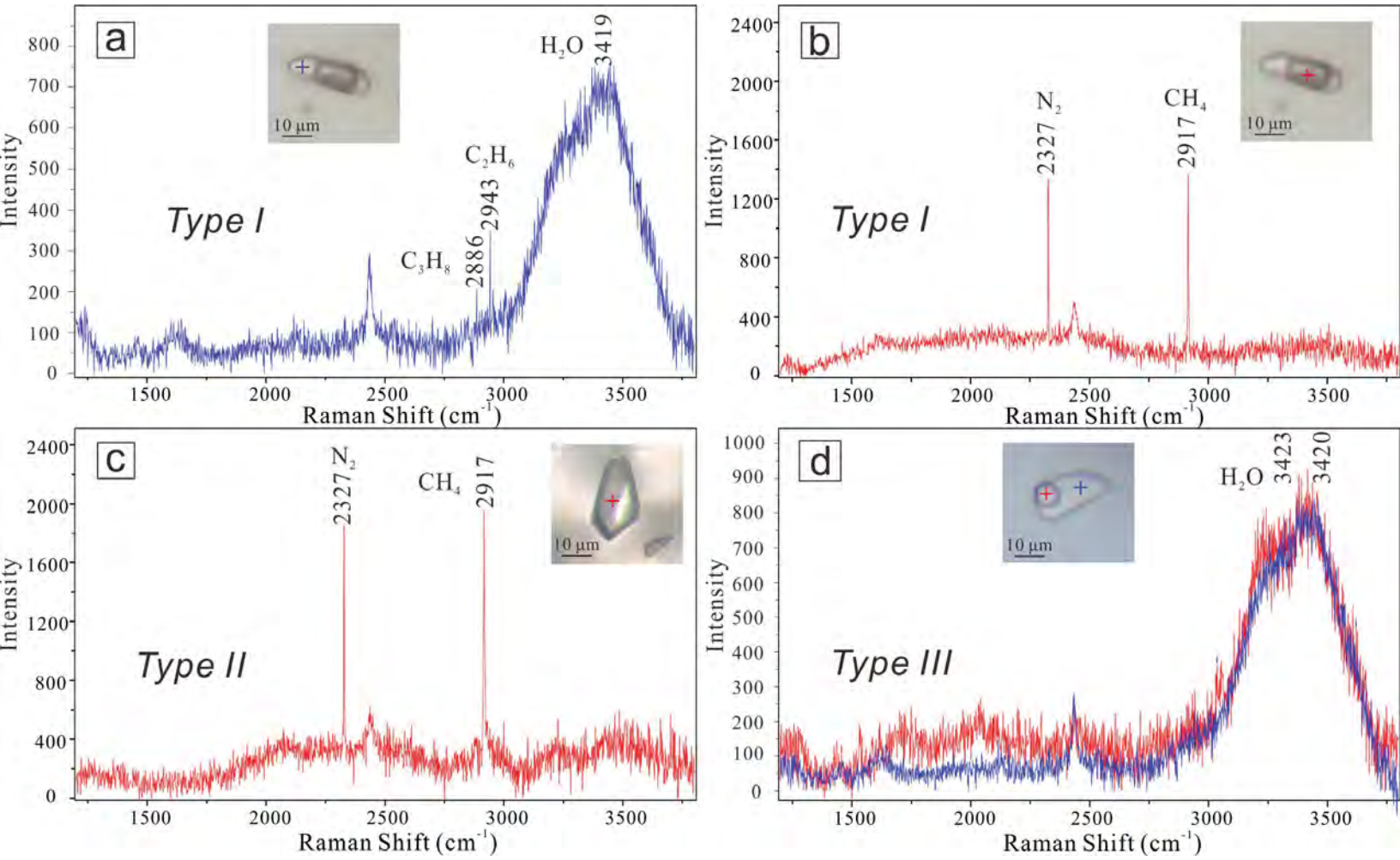
a
Type I
H2O
3419
C2H6
2943
2886
C3H8
10 μm
Intensity
Raman Shift (cm-1)
b
Type I
N2
2327
CH4
2917
10 μm
Intensity
Raman Shift (cm-1)
c
Type II
N2
2327
CH4
2917
10 μm
Intensity
Raman Shift (cm-1)
d
Type III
H2O
3423
3420
10 μm
Intensity
Raman Shift (cm-1)

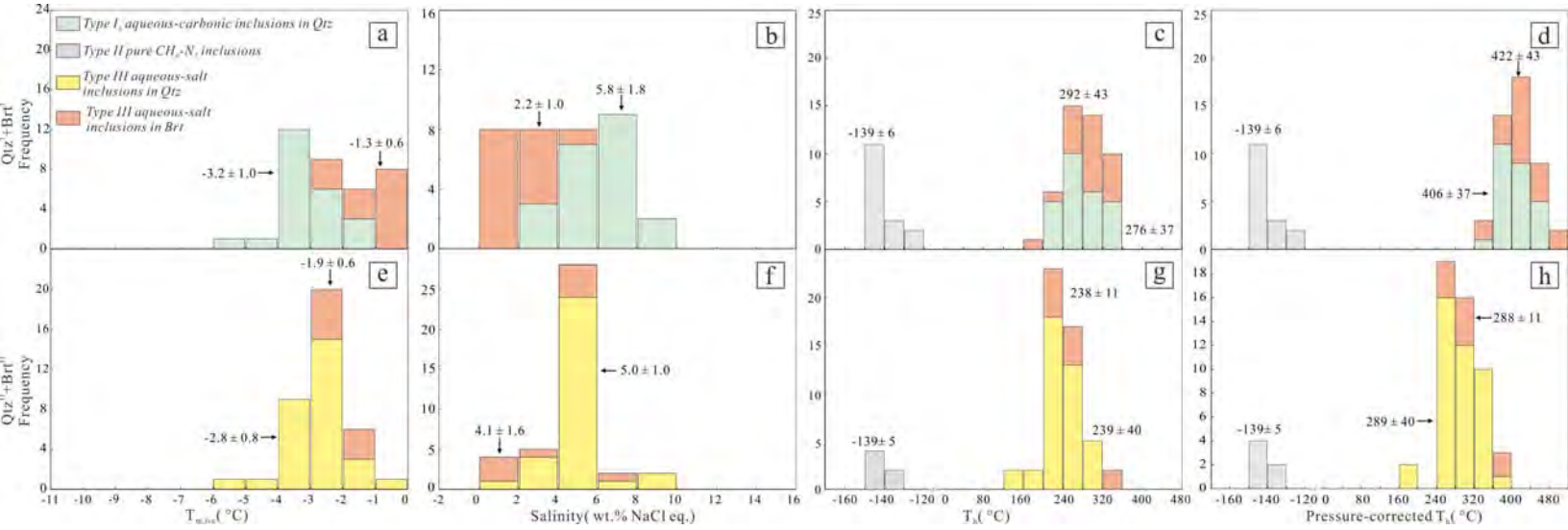
Type I, aqueous-carbonic inclusions in Qtz
Type II pure CH4-N2 inclusions
Type III aqueous-salt inclusions in Qtz
Type III aqueous-salt inclusions in Brt
a
b
c
d
e
f
g
h
-3.2 ± 1.0
-1.3 ± 0.6
2.2 ± 1.0
5.8 ± 1.8
-139 ± 6
292 ± 43
276 ± 37
422 ± 43
406 ± 37
-2.8 ± 0.8
-1.9 ± 0.6
4.1 ± 1.6
5.0 ± 1.0
-139± 5
238 ± 11
239 ± 40
289 ± 40
288 ± 11
Qtz'+Brt' Frequency
Qtz''+Brt'' Frequency
T m,ice (°C)
Salinity(wt.% NaCl eq.)
T h (°C)
Pressure-corrected T h (°C)

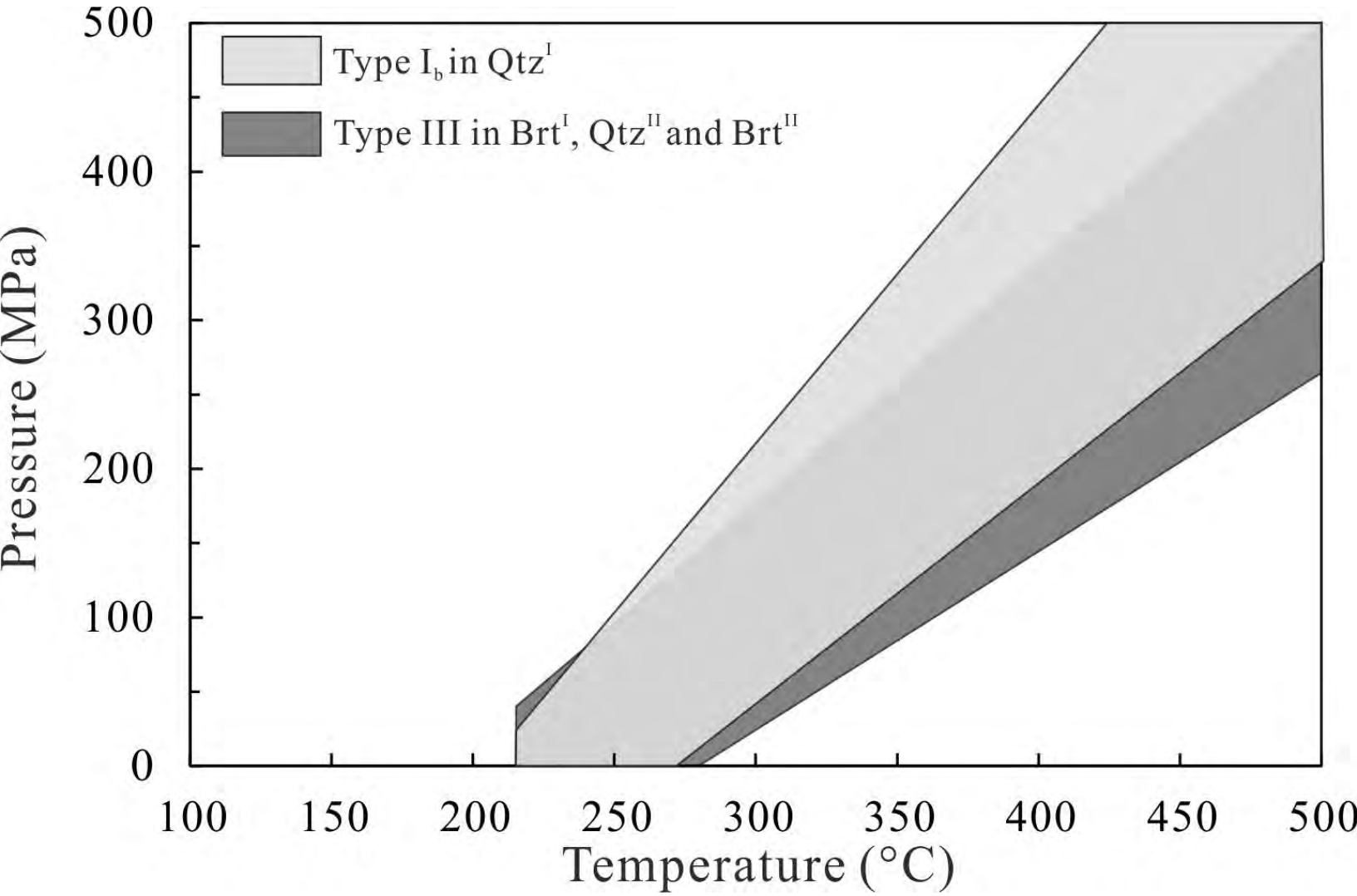
Type I_b in Qtz^I
Type III in Brt^I, Qtz^{II} and Brt^{II}
Pressure (MPa)
500
400
300
200
100
0
100
150
200
250
300
350
400
450
500
Temperature (°C)

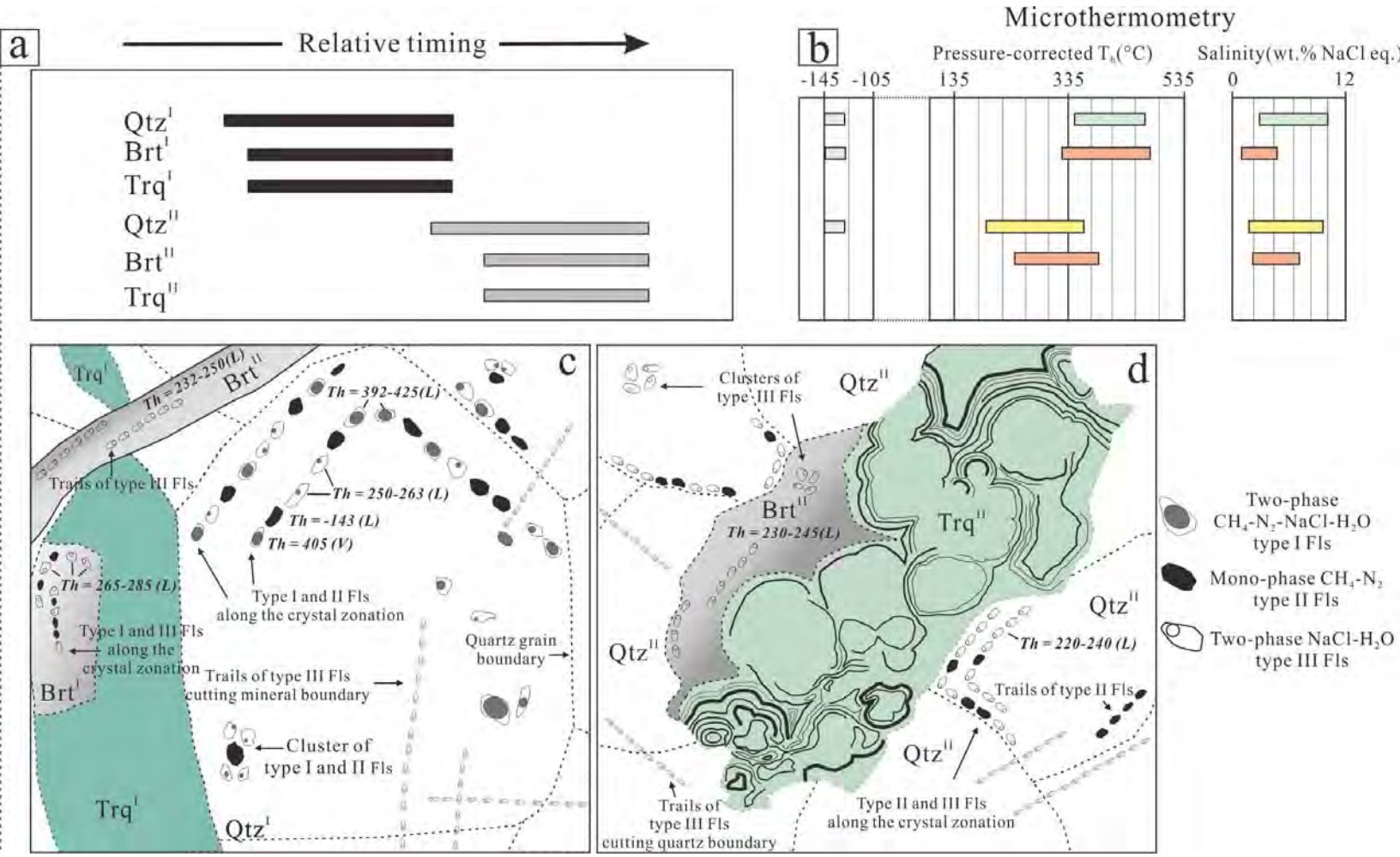
a
Relative timing
Qtz^I
Brt^I
Trq^I
Qtz^II
Brt^II
Trq^II
b
Microthermometry
Pressure-corrected T_h(°C)
-145 -105
135 335 535
Salinity(wt.% NaCl eq.)
0 12
c
Trq^I
Th = 232-250(L)
Brt^II
Th = 392-425(L)
Trails of type III Fls
Th = 250-263 (L)
Th = -143 (L)
Th = 405 (V)
Th = 265-285 (L)
Type I and II Fls
along the crystal zonation
Type I and III Fls
along the
crystal zonation
Quartz grain
boundary
Trails of type III Fls
cutting mineral boundary
Brt^I
Cluster of
type I and II Fls
Trq^I
Qtz^I
d
Clusters of
type III Fls
Qtz^II
Brt^II
Th = 230-245(L)
Trq^II
Qtz^II
Th = 220-240 (L)
Trails of type II Fls
Qtz^II
Trails of
type III Fls
cutting quartz boundary
Type II and III Fls
along the crystal zonation
Two-phase
CH4-N2-NaCl-H2O
type I Fls
Mono-phase CH4-N2
type II Fls
Two-phase NaCl-H2O
type III Fls

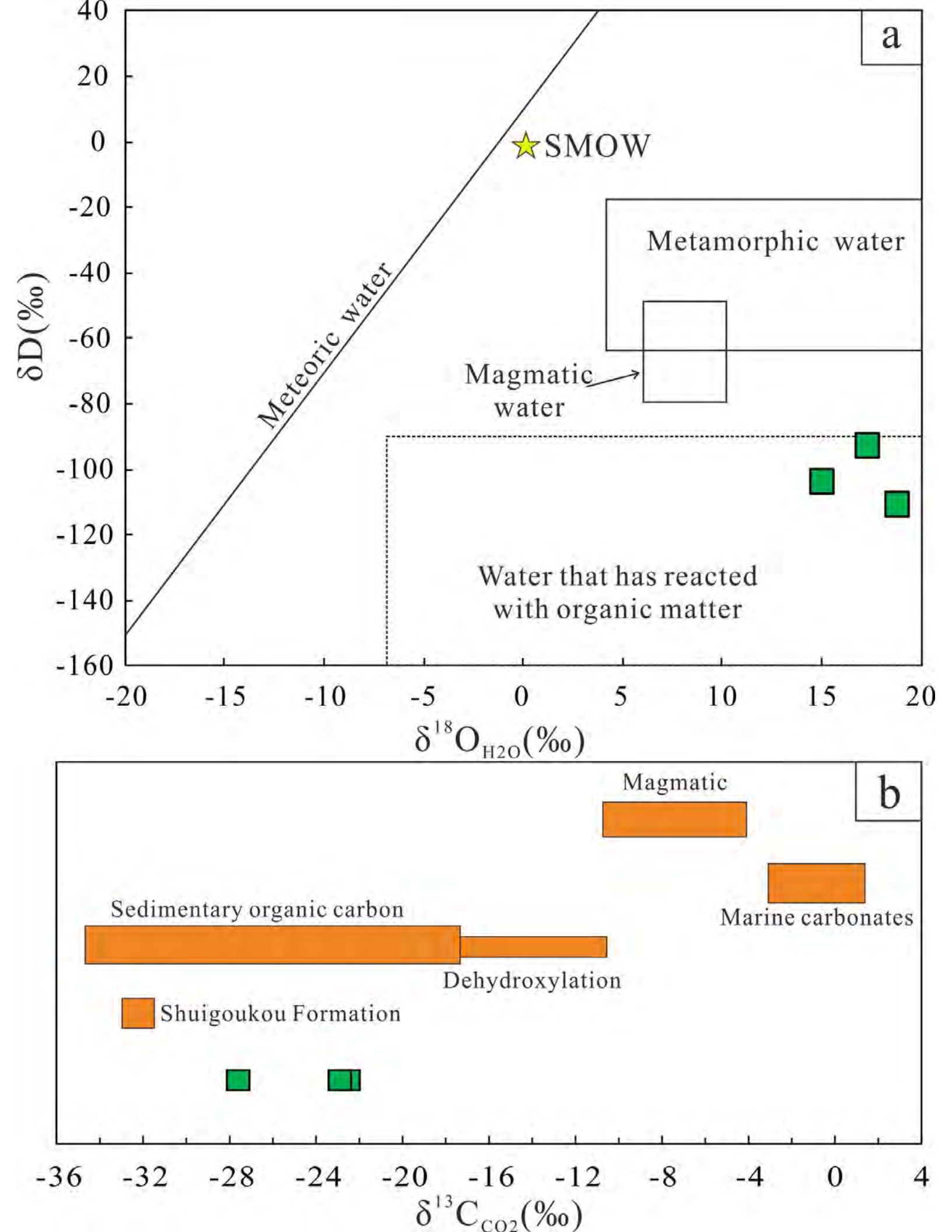
a
SMOW
Meteoric water
Metamorphic water
Magmatic water
Water that has reacted with organic matter
δD(‰)
$\delta^{18}O_{H2O}$(‰)
40
20
0
-20
-40
-60
-80
-100
-120
-140
-160
-20
-15
-10
-5
0
5
10
15
20
b
Magmatic
Marine carbonates
Sedimentary organic carbon
Dehydroxylation
Shuigoukou Formation
$\delta^{13}C_{CO2}$(‰)
-36
-32
-28
-24
-20
-16
-12
-8
-4
0
4